ENSEMBLE MONTE CARLO SIMULATION OF QUANTUM WELL INFRARED PHOTODETECTORS

A THESIS SUBMITTED TO
THE GRADUATE SCHOOL OF NATURAL AND APPLIED SCIENCES
OF
MIDDLE EAST TECHNICAL UNIVERSITY

BY

SEMA MEMİŞ

IN PARTIAL FULFILLMENT OF THE REQUIREMENTS
FOR
THE DEGREE OF DOCTOR OF PHILOSOPHY
IN
PHYSICS

MARCH 2006

Approval of Graduate School of Natural and Applied Sciences.

_____

Prof. Dr. Canan ÖZGEN

Director

I certify that this thesis satisfies all the requirements as a thesis for the degree of Doctor of Philosophy.

_____

Prof. Dr. Sinan BİLİKMEN

Head of Department

We certify that we have read this thesis and that in our opinion it is fully adequate, in scope and quality, as a thesis for the degree of Doctor of Philosophy.

_____	_____
Prof. Dr. Cengiz BEŞİKÇİ	Prof. Dr. Mehmet TOMAK
Co-Supervisor	Supervisor

Examining Committee Members:

Prof. Dr. Raşit TURAN	(METU, Physics)	_____
Prof. Dr. Mehmet TOMAK	(METU, Physics)	_____
Prof. Dr. Bilal TANATAR	(Bilkent University)	_____
Assoc. Prof. Dr. Hatice KÖKTEN	(METU, Physics)	_____
Asst. Prof. Dr Sadi TURGUT	(METU, Physics)	_____

I hereby declare that all information in this document has been obtained and presented in accordance with academic rules and ethical conduct. I also declare that, as required by these rules and conduct, I have fully cited and referenced all material and results that are not original to this work.

Name, Last name :

Signature :

ABSTRACT

ENSEMBLE MONTE CARLO MODELING OF QUANTUM WELL INFRARED PHOTODETECTORS

MEMİŞ, Sema

Ph.D., Department of Physics

Supervisor: Prof. Dr. Mehmet TOMAK

Co-Supervisor: Prof. Dr. Cengiz BEŞİKCİ

March 2006, 111 pages

Quantum well infrared photodetectors (QWIPs) have recently emerged as a potential alternative to the conventional detectors utilizing low bandgap semiconductors for infrared applications. There has been a considerable amount of experimental and theoretical work towards a better understanding of QWIP operation, whereas there is a lack of knowledge on the underlying physics. This work provides a better understanding of QWIP operation and underlying physics through particle simulations using the ensemble Monte Carlo method. The simulator incorporates Γ, L, and X valleys of conduction band as well as the size quantization in the quantum wells. In the course of this work, the dependence of QWIP performance on different device parameters is investigated for the optimization of the QWIP structure.

The simulations on AlGaAs/GaAs QWIPs with the typical Al mole fraction of 0.3 have shown that the L valley of the conduction band plays an important role in the electron capture. A detailed investigation of the important scattering mechanisms indicates that the capture of the electrons through the L valley quantum well (L-QW) affects the device performance significantly when Γ and L valley separation is small. The characteristics of electron capture have been further investigated by repeating the simulations on QWIPs for quantum well widths of 36 and 44 Å. The results suggest that the gain in the shorter well width device is considerably higher, which is attributed to the much longer lifetime of the photoexcited electrons as a result of lower capture probability (p_c) in the device.

The effects of the L-QW height on the QWIP characteristics have also been studied by artificially increasing this height from 63 to 95 meV in $Al_{0.3}Ga_{0.7}As$/GaAs QWIPs. The increase in the L valley (L-QW) height resulted in higher pc and lower gain due to high rate of capturing of these electrons when Γ and L valley separation is small.

Keywords: Infrared detectors, quantum well, Monte Carlo simulation.

ÖZ

KUANTUM KUYULU KIZILÖTESİ FOTODETEKTÖRLERİN MONTE CARLO MODELLEMESİ

MEMİŞ, Sema
Doktora, Fizik Bölümü
Tez Yöneticisi: Prof. Dr. Mehmet TOMAK
Yardimcı Tez Yöneticisi: Prof. Dr. Cengiz BEŞİKCİ

Mart 2006, 111 sayfa

Kızılötesi uygulamalarda, kuantum kuyulu kızılötesi fotodedektör (KKKF) yapıları düşük bant aralıklı yarı iletkenlerinin kullanıldığı geleneksel dedektörlere güçlü bir alternatif olarak son yıllarda ortaya çıkmıştır. KKKF operasyonlarını daha iyi anlamaya yönelik oldukça fazla deneysel ve teorik çalısmalar bulunmaktadır, fakat temel fizik bilgileri halen eksiktir. Tez çalışmasında Monte Carlo methodu kullanılarak KKKF operasyonun daha iyi anlaşılması ve parçacık similasyonlarını içeren fiziği vurgulaması sağlandı. Bu simulator kuantum kuyulara iletken bandının Γ, L ve X vadilerinin yanı sıra boyut kuantalaşması ilave edilmiştir. Bu çalışma alanında, KKKF yapılarını optimal yapmak için KKKF verimliliğinin farklı cihaz parametrelerine bağımlılığı araştırıldı.

Tipik mol oranı 0.3 olan A1GaAs/GaAs KKKF'ler üzerinde yapılan simulasyonlar iletkenlik bandındaki L vadisinin elektron yakalanmasında önemli bir rol oynadığını göstermiştir. Önemli saçılım mekanizmalarının detaylı incelenmesi, Γ ve L vadisi arasındaki mesafe küçük olduğunda, L vadisi kuantum kuyusu (L-KK) içinden electron yakalanmasının, cihaz randımanını önemli ölçüde etkilediğini göstermektedir. Elektron yakalanmasının karakteristiği, kuantum kuyusu eni 36 ve 44 Å olan KKKF'ler için simulasyonları tekrarlayarak da incelenmistir. Sonuçlar, daha kısa kuyu enli cihazlardaki kazancın farkedilebilir ölçüde daha yüksek olduğunu önermektedir ki bunu, fotouyarılmış elektronların, cihazdaki daha düşük elektron yakalama olasılığının sonucu olarak çok daha uzun ömürlü olmasıyla ilişkilendirebiliriz.

Ayrıca, L-KK yüksekliğinin KKKF karakteristiği üzerindeki etkileri de, bu yüksekliğin $A1_{03}Ga_{0.7}As$/GaAs KKKF'lerde suni olarak 63 meV'tan 95 meV'a suni olarak yükseltilmesiyle çalışılmıştır.

Anahtar Kelimeler: Kızılötesi algılayıcılar, kuantum kuyusu, Monte Carlo benzetimi.

ACKNOWLEDGMENTS

I would like to express my deepest gratitude to Prof. Dr. Mehmet Tomak for his excellent supervision, encouragement, continuous support, positive attitudes and invaluable guidance, for the trust and freedom he gave me during this work. He is not only a great scientist with deep vision but also and most importantly a kind person.

I am very grateful to Prof. Dr. Cengiz Beşikçi who has given me the chance to participate in his group. I always appreciate his unconditional guidance and help throughout this work. I wish also thank Dr. Arzu Onay Beşikçi for all of her support and helps. I would also like to thank Oray Orkun Cellek for providing the ensemble Monte Carlo simulation program that I have used in my thesis and for his generous input and constructive criticisms.

I would like to thank Prof. Dr. Bilal Tanatar and Assoc. Prof. Dr. Hatice Kökten for serving on my progress committees, providing indispensable advice, and invaluable collaboration. I wish to thank Prof. Dr. Tanatar for his help on the calculation of the screened two-dimensional polar optical phonon scattering rates. My special thanks go to Assoc. Prof. Dr. Hatice Kökten for encouragement and friendship. I would also like to thank my thesis defence committee members Prof. Dr Raşit Turan and Asst. Prof. Dr Sadi Turgut for their time and for continuous help throughout my education.

I must thank Emre Öncü for his collaboration during the early stages of my Ph.D. study. I am also very grateful to Umut Bostancı for his good friendship and contiuous help. I also want to thank to Evrim Çolak for his encouragements

and helps. Many thanks extend to our research group members, Özlem Ersagun, Melih Kaldırım, Gökhan Demirci, Selçuk Özer,U. Süleyman Eker, Burak Aşıcı, Ümid Tümkaya, Hasan Koçer and Özgür Şen for creating a friendly working environment.

I wish to thank all collegeous and friends. Many thanks to six year officemate, Aybike Çatal Özer for a lot of good time together and for close friendships and her support. She is among the best things ever happened to me. I want to also thank two of my best friends Sevgi Özdemir Kart and her husband Hasan for their encouragements, helps and good friendships. Thanks to Emine and Uğur Serincan for their good and close friendships since 1992 and all helps, especially on computers. I owe thanks to Mustafa Arıkan, Bülent Aslan Mustafa Kulakçı and Hülya Atmacan for their helps, support and friendship.

I would like to thank my best friends Gül E. Polat, Canan Öktemgil Turgut, Sibel Ünlü, Ezgi Şenol and Meryem Yücel for their continuous support and encouragements and their love.

Above all, I would like to thank my family for their unlimited love and support. I dedicate this thesis to my mother.

To My Mother

TABLE OF CONTENTS

LIST OF FIGURES

FIGURE

LIST OF TABLES

TABLE

CHAPTER 1

INTRODUCTION

Recent advances in computer technology increase the importance of numerical methods and simulations in scientific investigation, and they complement theoretical and experimental approaches. The device modeling methods with simulations save the cost of discovery and time by using computer design where devices are characterized, and optimized before beginning the expensive experimental processes of fabrication, characterization and testing.

With the discovery of the infrared radiation in 1800 by Herschel and then, the discovery of thermoelectric effect in 1830 by Seeback [1], infrared detector has added a dimension to human-sight. Infrared detectors are used widely as thermal sensors in military applications, security, medical imaging, fire alarms, scientific research etc. [2-5]. Quantum well infrared photodetector (QWIP) technology has been developing as a potential alternative to the conventional photodetectors since 1977 [6]. Although there are large amount of experimental and theoretical studies on QWIPs, there are gaps in understanding of their operation in microscopic level. The modeling of QWIP is important in terms of understanding its operation and of optimization as a detector before fabrication.

The well-known device modeling techniques in electronic and optoelectronic devices are the drift diffusion models, the hydrodynamic models and the Monte Carlo (MC) simulation. Kane *et al*. presented 3D carrier drift model for QWIPs in 1992 [7]. In their model, the 3D density was calculated by treating the barriers as a bulk semiconductor and the 2D doping density N_D equaled the electron density within a given well. It is expected that this model is valid under small bias since the Fermi level is determined by well doping. This model was improved by Man and Pan in 1995 by with including different carrier temperatures or Fermi levels. In their model, the barrier hot electrons were related with the 2D well electron temperature and applied electric field [8]. On the other hand, Chu *et al*. calculated the 3D barrier electron Fermi level by balancing the tunneling escape rate in 1987 [9]. These two latter models resulted in better fitting of experimental results than the former one.

Ershov *et al*. [10, 11] modeled the QWIP by using self-consistent drift-diffusion model. In this numerical model, the Poisson equation, the continuity equation for electrons in the barriers and the rate equation for electrons in the barriers was solved self-consistently. Including the Poisson equation is necessary in a MQW structure due to non-uniform electric field (E-field) distribution throughout the device. Ershov *et al.* presented nonlinear photoconductivity effects at high excitation power in QWIPs due to a redistribution of the electric potential at high power which leaded to a decrease of electric field in the bulk of QWIP [12]. They stated that the QWIP capacitance shows unusual behavior as a function of voltage and frequency deviating far from the constant geometric capacitance value [13].

Thibaudeau *et al*. presented a numerical model which involved elementary mechanisms, e.g. injection at the contact and balance between capture and emission in each well, in a self-consistent way [14]. This model allows the electric field to be non-uniform and self-consistently determined by the Gauss law.

Ryzhii derived an analytical model [15] where intersubband electron transitions and tunneling injected electrons were used. In this model, Poisson's equation and an equation governing the electron balance in the quantum well were included. The dark current and resposivity were obtained as function of QWIP parameters in an analytical form. Ryzhii *et al*. improved their self-consistent analytical model [16]. This model took into account electron thermionic emission from the quantum wells, thermionic injection from the emitter contact, and features of transport and capture in the self-consistent field in the QWIP active region. They obtained the electric field and charge distributions as well as dark current-voltage charecteristics and confirmed that the effect of the emitter contact substantially weakens with increasing number of QWs in the QWIP structure. They also presented an analytic model for dual band QWIPs [17]. Ryzhii and Liu presented a self-consistent analytical model where they showed that the electric field and space-charge distribution in the QW structure were nonuniform in general [18].

The drift-diffusion model is a simple transport model which may lose its reliability for complex structures like quantum well infrared photodetectors (QWIPs) since this model assumes the carrier velocity to be a function of local electric field and it is insufficient in describing carrier flow in the presence of large electric field gradients [19, 20]. The hydrodynamic transport models where the mobility and diffusivity are functions of the local electron energy give more reliable results. However, the application of these methods is complicated [21].

MC methods are stochastic techniques which are based on the use of random numbers and probability statistics for investigating problems. These techniques are used widely from economics to nuclear physics. The ensemble Monte Carlo (EMC) technique enables one to simulate large numbers of carriers in a device by tracking the behavior of each carrier in momentum and position space at a microscopic level. This method is suitable for optimizing device parameters in terms of material system as well as material specifications; length of

heterostructures, doping etc. The feasibility of EMC technique increases with development of computer capacity.

EMC simulation is an effective tool for investigations on the QWIP operation and characteristics. The advantage of MC technique in the investigation of device operation is to obtain detailed results with higher correctness [22]. The main objective of working on device operation is optimization of the device parameters. There are extensive studies on the QWIP MC simulations [19, 23-31].

Artaki and Kizilyalli presented MC simulations of electron transport in QWIPs [23]. They studied the collection efficiency of the photoexcited electrons at 70 K as a function of bias as well as the response time. In their simulators, the transition rates from a continuum state to a bound state through the emission or absorption of a polar optical phonon were calculated for both Γ and L valleys ($\Gamma_{3D} \Rightarrow \Gamma_{2D}$, $L_{3D} \Rightarrow L_{2D}$). However the bound state electrons were not simulated.

QWIPs were studied with MC simulation mainly by Ryzhii's group [19, 26-29, 32]. They investigated QWIP characteristics, in particular their ultrafast electron transport properties. In their work, the interaction probability of Γ electrons with QW's (i.e. reflection, transmission or capture of electrons) was treated quantum mechanically while the transport of L and X electrons was considered classically. These studies have clarified various important features of QWIP operation. However, the models should be improved further for better understanding of QWIP operation and characteristics through detailed MC simulations.

In the scope of this work, QWIPs are simulated by using an EMC simulator. The main objective is to resolve the effects of various parameters on QWIP characteristics as well as explaining the underlying physics. The ensemble

Monte Carlo program which is used in this work is developed by O.O. Cellek [33-35].

This thesis is arranged as follows: Chapter II is devoted to the general discussion of the infrared detector technology. In chapter III, the concept of QWIP is given. Chapter IV describes the ensemble Monte Carlo technique for QWIPs and modeling approach in detail. In Chapter V, the results of our simulation in QWIPs are discussed. Finally, conclusion and suggestion for further study are given in chapter VI.

CHAPTER 2

INFRARED DETECTORS

2.1 Introduction

The light we see with our eyes is really a small portion of Electromagnetic spectrum. Infrared radiation is located just beyond the red side of the visible spectrum. Infrared radiation has a wavelength range of 0.7 μm -1000 μm.

Infrared radiation was first discovered in 1800 by W. Herschel, who was trying to determine the part of the visible spectrum with minimum associated heat content in connection with his astronomical observations. In 1847, A. H. L. Fizeau and J. B. L. Foucault showed that infrared radiation has the same properties as visible light, being reflected, refracted, and capable of forming an interference pattern. Peak emission from the objects at room temperature occurs at a wavelength of 10 μm.

The infrared spectrum is usually subdivided into the far infrared FIR (>25μm), very long wavelength infrared VLWIR (12-25μm), long wavelength infrared LWIR (8-12μm), mid wavelength infrared MWIR (3-5μm), short wavelength infrared SWIR (1.5μm-3μm) and near infrared NIR (0.7-1.5μm) [36]. Figure 2.1 shows the atmospheric transmission over a spectral range from 0.7 to 15μm [37].

The detector technology is mainly focused on the two atmospheric windows, MWIR (3-5μm) and LWIR (8-12μm) where the highest atmospheric transmission occurs and radiated energy of an object mostly lies in this range at room temperature, e.g. for the human body at 310 K, the wavelength of peak thermal radiation is 9.3 μm.

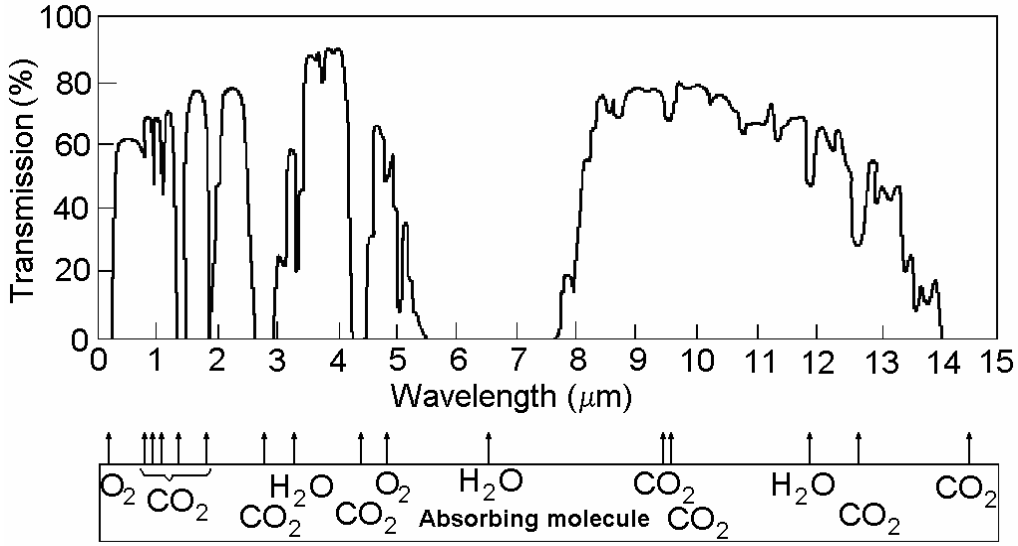

Figure 2.1: Atmospheric transmission spectrum and absorbing molecules. Spectrum was measured at sea level and through 6000 ft horizontal path [37].

Infrared technology is widely used in both civil and military applications. As a detector, it can be used in night vision equipment, when there is insufficient visible light to see an object. The radiation is detected and turned into an image on a screen, enabling the user to acquire thermally significant targets, such as humans and vehicles. Fire fighters use infrared imaging equipment when working in smoke-filled areas since smoke is transparent to infrared radiation. Remote determination of an object's temperature is called thermographing (thermal imaging). Infrared data transmission is employed in short-range communication among computer peripherals and personal digital assistants (e.g. home-entertainment remote-control boxes, wireless local area networks, links between notebook computers and desktop computers, cordless modems). Infrared radiation spectroscopy has enabled researchers to study the composition

of organic compounds. It determines a compound's structure and composition based on the percentage transmission of infrared radiation through a sample.

Infrared detectors [38-42] are divided mainly into two branches with respect to the physical mechanism used in detection, namely photon detectors and thermal detectors. A photon detector's working principle is a selective wavelength dependence of response per unit incident radiation power. Photon detectors are preferable with perfect signal to noise ratio performance and remarkably fast response. To avoid the detoriating effects of the ambient conditions, they require cryogenic cooling which make them bulky, heavy and expensive. Contemporary photo detector technologies can be listed as; intrinsic detectors (e.g. HgCdTe, InGaAs, InSb, PbS, PbSe), extrinsic detectors (e.g. Si:As, Si:Ga), photoemissive detectors (e.g. metal silicide Schottky barriers), quantum well infrared photodetectors, QWIPs (e.g. GaAs/AlGaAs, InGaAsP/InP, GaInP/InP, InGaAs/GaAs, GaInAs/InP), quantum wire photodetectors and finally quantum dot infrared photodectors, QDIPs (e.g. InAs/InGaAs, InGaAs/InGaP, InGaAs/GaAs, InAs/GaAs, Ge/Si).

Using thermal detector is another alternative method for detection of infrared radiation. In thermal detectors, the incident radiation is absorbed to change the temperature of material and resultant change in some physical properties is measured to generate an electrical output. The detector equipment is suspended on legs, which are connected to a heat container. Different types of thermal detectors are bolometers, pyroelectric detectors, thermopiles and pneumatic detectors. Thermal detectors are widely used commercially since they typically operate at room temperature and they have monolithic design of the complete sensor unit including the readout circuit, which permits a low price per camera system. A major drawback of thermal detectors is their slow response. Their modest sensitivity is another disadvantage.

Today, there are four primary photodetectors technologies employed in thermal imaging systems. These are mercury cadmium telluride (MCT), QWIP, and indium antimonite and micro-bolometer / pyrometer focal plane arrays.

2.2 Thermal Detectors

When Herschel discovered the infrared radiation in 1800, he was using a simple type of thermal detector, a liquid in a glass thermometer. In 1921 Seebeck discovered the thermoelectric effect and, then demonstrated the first thermocouple. The first thermopile was constructed by Nobili in 1829 [43]. After that, in 1833, Melloni modified thermocouple design by using bismuth and antimony [44]. This was followed by a resistive metal bolometer invented by Langley in 1880 [45].

The most significant advance of thermal detectors is that they are relatively cheap and, they can be manufactured in large quantities. The infrared flux is detected at each pixel location by measuring an absorber temperature change caused by the amount of IR energy absorbed in the device. Integration with the readout circuit in a small pixel pitch is achieved by keeping a good thermal insulation between the absorber and the readout which acts as a heat sink. A thermal detector consists of three main parts; the absorber for the infrared radiation, the thermal insulation part (i.e. membrane) and the temperature detector. The absorber can be a finely subdivided metal such as platinumblack. It also can be based on interferometric structure.

To achieve high sensitivity it is necessary to have good insulation between the thermal detector element and the detector substrate. Because of compatibility with silicon processing, silicon nitride or silicon dioxide are mostly used as membrane. The temperature detector part is capable of detecting extremely small temperature changes resulting from exposure to the infrared radiation from the object and subsequent absorption.

Thermal detectors have lower sensitivity compared to photon detectors, and their sensitivity to changes on the radiated wavelength is low so they are called broadband detectors [46], as shown in Figure 2.2. Due to their broadband response, these detectors can be favored in some applications where the broader response is required to detect features, like gases in the atmosphere. However, for standard imaging systems, the broader response can be a drawback, since broadband detectors are sensitive to radiation outside the atmospheric transmission window, as well. Thermal detectors are relatively slow when compared with photon detectors, since they must reach thermal equilibrium when the target temperature changes rapidly. Some examples of widely used thermal detectors are explained briefly below.

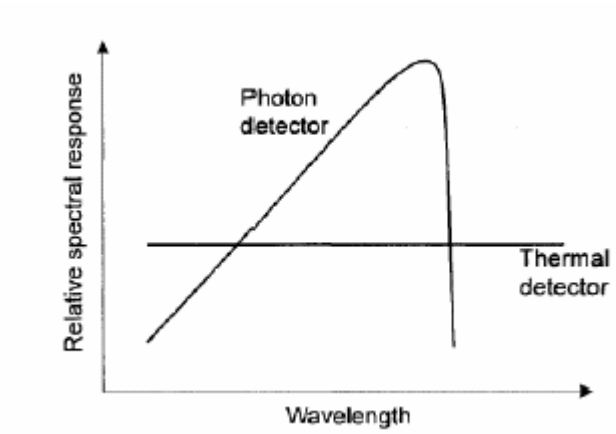

Figure2.2: Photon detector versus thermal detector response [46].

2.2.1 Thermopiles

Thermopiles [40] are the oldest type of infrared detectors. They utilize thermo-electromotive force generated between two different types of conductors. A thermopile consists of one or more thermocouples connected in series, which generate thermo-electric emf when heated. It is usually arranged in radial pattern so the hot junction forms a small circle, and the cold junctions are maintained at the local ambient temperature. Thermopiles are made from both metals and semiconductors. Highly developed thin film thermopiles succeed response times

in the 10 to 15 ms range. Thermopiles can stand to high temperatures and are the best choice for broadband thermometers. A substrate temperature controller is used to avoid ambient temperature fluctuations for low temperature work.

2.2.2 Bolometers

Bolometers are resistance thermometers employed for sensing radiation. The bolometer was invented by Langley in 1860 [45]. It consisted of a radiation-sensitive resistance element in one branch of a Wheatstone bridge, i.e. radiation was detected with changes in the electrical resistance of the element. The radiation sensitive element may be a platinum strip, a semiconductor film, or any other material whose resistance can response to slight changes in the amount of radiant energy falling on it. The detection spectra range from light waves to microwaves. Thermal phonons are generated by the incident photons whose energy is transferred to the absorber. They change the current flowing through a thermistor. Bolometers are capable of responding to a range of wavelengths without significant variation in responsivity. Their sensitivity is high at room temperature, which enables imaging applications. Bolometer arrays have become the focus of most uncooled detector development. Microbolometer FPAs are based on silicon technology. The main advantage of microbolometer detectors is the omission of a cryogenic cooler system. However, the main drawback is the need for a tight temperature control of the environment for absolute measurements.

2.2.3 Pyroelectric Detectors

When infrared radiation is incident on the detector, temperature changes are generated in the crystal [40]. An electrical charge is then generated on the surface of the crystal proportional with the amount of temperature change. Pyroelectric detectors [38] depend on the change in surface charge in response to radiation. Reaching thermal equilibrium is not important when the target temperature changes, since it responds to the microscopic effects of the

incoming radiation. The incoming radiation must be chopped, and the detector output cannot be used directly. A chopper is a rotating or oscillating shutter employed to provide AC output from the sensor. The detector output is read similar as in the case of reading the charge of a capacitor, which must be sensed with a high impedance circuit. Pyroelectric detectors include radiation absorbent coatings so they are suitable for broadband detection. Selecting the coating material with appropriate characteristic determines the response. Like photon detectors, pyroelectric detectors have thermal drift that can be overcame by thermistor, temperature regulation, auto null circuitry, chopping, and isothermal protection. PbS has the greatest sensitivity. Being capable of extremely rapid response and insensitive to DC effects, they are often used in industrial radiometric systems and in the analysis of infrared lasers.

2.2.4 Pneumatic Detector

There are two types of pneumatic detectors [40]: Golay cells and capacitor microphones. In Golay cells, the sealed Xenon gas expands when warmed with incident infrared radiation. The resultant variation of pressure shifts a mirror located between a light source and a photocell, varying the amount of light entering the photocell and thus changing the output of the photocell. In capacitor microphones, a capacitor film is deflected due to the varying expansion of the gas, which in turn produces the variation in the electrostatic capacity.

2.3 Photodetectors

Photodetectors [38, 39] convert a light signal to an electrical quantity such as a voltage or current. The photoexcitation occurs when the radiation interacts directly with the constituents of the material. The detector must be cooled down to low enough temperature, so that the number of thermally excited carriers across the bandgap is less significant. A Dewar can be used to keep the temperature low, which increases the system cost and restricts the practicality of usage. The extrinsic photon detectors require more cooling than intrinsic ones

with the same long wavelength limit. The spectral absorption and photoexcitation are primary parameters determining the sensitivity of photon detectors. The spectral response of photon detector depends on photon wavelength.

The quantum efficiency is a measure of how many electrons are produced for every photon incident on the photosensitive surface. It is given by

$$\eta = \frac{n_e}{n_{ph}} 100\% \tag{1.1}$$

where n_e is the number of photoelectrons generated and n_p is the number of incident photons. The quantum efficiency is in the range of 5 to 30% for a photodetector.

Photodetectors can be subdivided into three branches; photoconductive, photovoltaic and photoemissive devices, depending on the method of the electrical signal developed. In photoemissive photodetectors, electrons are ejected from a photoemissive surface irradiated with light. Photons must have enough energy to overcome the binding energy of the electrons. Minimum energy required to eject an electron is the energy corresponding to the difference between the top of valence band and the ionization energy of material. Photomultipliers are commonly used for low light level applications (with alkali materials-Na, Li, Cs and alloys).

Photovoltaic intrinsic detector structure is based on a p-n junction device. The reflective coating on the bottom of the detectors is used to increase photon absorption. The potential barrier of the p-n junction leads to the photovoltaic effect under IR radiation. An incident photon generates electron-hole pairs when its energy is higher than the band gap energy of the junction. The amount of the photon-excited current is called photocurrent. Photovoltaic devices operate in the diode's reverse bias region in order to minimize the dark current flow

through the device. The noise of photovoltaic detectors is low. Si, Ge, GaAs, InSb, HgCdTe and PbSnTe are examples of high performance photovoltaic detectors.

Photoconductive detector mechanism relies on producing conductance change under the IR radiation. The free carriers generated by the photons cause increase of the conductance of photoconductive material under applied bias. There are both intrinsic and extrinsic types of photoconductors. The doping of intrinsic semiconductor enables us to control the spectral response of a semiconductor material. For example, photoconductors can even operate in LWIR detection. In the intrinsic semiconductor, the absorbed photon generates holes and electrons. In the extrinsic one, the photon is absorbed by the impurity, and only majority carriers are excited. The resultant current magnitude depends on photon flux under the applied bias. The photoconductive gain is the ratio of carrier lifetime to transit time, where carrier lifetime depends on the capture probability. Common gain values are on the order 0.5 and higher. The photoconductive detector consumes considerable. Therefore, photoconductive detectors are not suitable for large IR array application. The generation-recombination noise exists in photoconductive detectors in addition to thermal and other kinds of noise sources. InSb, PbSb, PbSe, QWIP, HgCdTe and PbSnTe are examples of widely used photoconductors. The ternary compounds HgCdTe and PbSnTe can be applied as photoconductive detectors as well as photovoltaic detectors.

When photoconductive detectors are compared with photovoltaic detectors; the latter provide a better signal to noise ratio, simpler biasing and better responsivity. However photovoltaic detectors are more fragile, susceptible to electrostatic discharge and to physical damage due to handling.

In an extrinsic detector, a deep level is introduced in the bandgap, photons can cause transitions from these levels to the conduction band. Extrinsic detectors are mostly based on Si or Ge doped with impurities such as boron, arsenic and gallium. They are important for the detection of long wavelength IR radiation.

The biggest difference between intrinsic detectors and extrinsic type detectors is the operating temperatures. Extrinsic type detectors must be cooled down to the liquid helium temperature. It is possible to produce extrinsic detectors operating at low temperatures up to a wavelength of 120 μm.

2.3.1 Mercury Cadmium Telluride Detectors

HgCdTe (MCT) was invented in 1959 by a research group led by Lawson [47]. MCT has been intensively developed over the past forty years and today it is the most widely used infrared detector material for thermal imaging applications.

MCT is a ternary semiconductor compound. Its wavelength cutoff varies with the alloy composition. The detector is composed of a thin layer (10 to 20 μm) of MCT with metalized contact pads which define the active area. Photons excite electrons into the conduction band when their energy is larger than the semiconductor band gap energy, therefore increasing the conduction of the material. The desired wavelength (in the range of 0.7-25 μm) of peak response can be achieved by changing $Hg_{1-x}Cd_xTe$'s band gap energy by varying the alloy composition (x). Temperature dependence of CdTe and HgTe band gaps are different. The band gap of HgTe increases with temperature while that of CdTe decreases. During the tailoring of band gap of MCT, temperature dependence of the structure must be taken into account. Both photoconductive and photovoltaic types are available. Photovoltaic MCT is the most frequently used detector material in the 3-5 μm and the 8-12 μm wavelength bands. MCT has been developed into three generations of detector devices parallel with improvement in the crystal growth technology. The first generation is linear array of photoconductive detectors which are still used today. The second generation is two dimensional arrays of photovoltaic detectors which have increasing volume of production. Third generation is the two-color detectors, avalanche photodiodes and hyperspectral arrays which have been developing in demonstration programs.

MCT is a direct bandgap material with high absorption coefficient which is considered as the major advantage in IR detection world. MCT is an intrinsic detector so the cooling limit is not as low as for extrinsic detectors. They have moderate dielectric constant, index of refraction and moderate thermal coefficient of expansion. Moreover, availability of wide bandgap lattice-matched substrates are other advantages of this detector technology [48]. Photoconductive MCT can be preferred in high performance applications such as thermal imaging and radiometry since they provide better sensitivity, faster response and lower bias voltage [38].

One main drawback of this technology is the difficulty in growing HgCdTe material, due to the high vapor pressure of Hg. Nonuniformity and fragility are additional limitations of MCT. These problems have encouraged the development of alternative detector technologies.

2.3.2 IR Detectors Based on Low-Dimensional Semiconductor Heterostructures

Quantum Well Infrared Photodetectors: Chapter III is devoted to the quantum well infrared photodetectors (QWIPs)

Quantum Wire Infrared Photodetectors: The first electronic and optical studies on quantum wire Infrared photodetectors (QWR) were done by Sakaki in 1980 [49, 50]. The additional quantum confinement of carriers results in significant improvement in the device performance [51]. The QWR photodetector have different quantum confinement structures: the sidewall quantum well (SQWL), the vertical quantum well (VQWL), and the planar quantum well (PQWL). The AlGaAs/GaAs QWR infrared photodetectors which were based on a V-grooved substrate was demonstrated by X. Q. Liu *et al*. [52].

Quantum Dot Infrared Photodetectors : Being not sensitive to normal incident light, due to dipole selection rule, there is a limitation of n-type doped

QWIPs which causes poor photoresponse. To solve the problem, the alternative structures with the lateral electron confinement were developed. Quantum dot infrared photodetector (QDIPs) is an example. It has carrier confinement in all three directions. QDIPs are also different from QWIPs in terms of having a broader infrared response range since several discrete states are created in the self-assembled QD in addition to the inhomogeneous growth of QDs, which broadens the response range to the longer wavelengths. Figure 2.3 shows the subband energy states. Transition to the wetting layer or to the continuum states will result in infrared detection. With suitable barrier material, height and thickness are selected in addition to the QD size to tune the detection range.

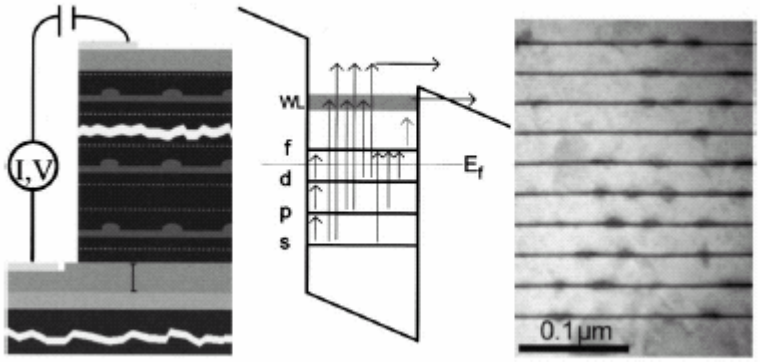

Figure 2.3: Schematic of a QDIP structure (left), of its energy diagram (centre), and cross-section TEM view of the bottom ten layers of a 50-layer InAs/GaAs QDIP device [53]

InGaAs/InGaP QD detector for MWIR detection was demostrated by Kim *et al*. [54-56]. In the structure, InGaAs QD was formed by intrinsic strain due to a lattice mismatch. InAs/GaAs based on QD detector with ~5 μm peak wavelength response was fabricated by H .C. Liu *et al*. [53].

CHAPTER 3

QUANTUM WELL INFRARED PHOTODETECTOR

3.1 Introduction

The quantum well infrared photodetector, QWIP, is a semiconductor infrared photon detector depending on intersubband absorption within either the conduction band or valence band. The idea of using a quantum well for infrared detection was first presented by Esaki and Sakaka in 1977, as an alternative to conventional intrinsic infrared photodetectors [6]. A quantum well consists of two or more materials different band gaps. In basic structure (type I), a lower bandgap material (i.e. GaAs) grown between two larger bandgap materials (i.e. AlGaAs) as seen Figure 3.1. The height of the well is determined by the relative composition, x. The numbers of bound energy levels are determined by the length and depth of the well. Intersubband transitions enable us to fabricate IR detectors for the 3-5 and 8-12 μm atmospheric windows. The operation of a QWIP can be explained by using the basic principles of quantum mechanics.

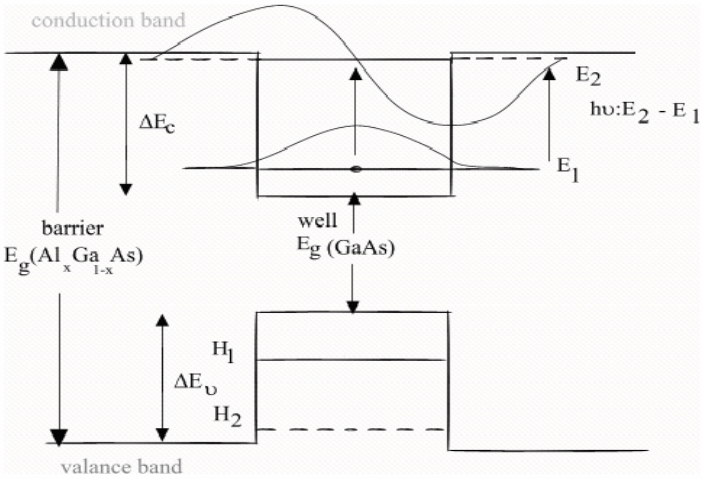

Figure 3.1: Operation of a QWIP

A quantum well is treated as a particle in a box problem which can be solved by the time-independent Schrödinger equation. The solution of Schrödinger equation for a real device is not straightforward. For the sake of simplicity, if infinitely high barriers and parabolic bands are assumed; the wavefunctions and the energy levels are given by

$$\psi_n(\vec{x},\vec{y},\vec{z}) = \sqrt{\frac{2}{L_z A}}\sin(\frac{n\pi z}{L_z})\exp(ik_x x + ik_y y), \tag{3.1}$$

$$E = \frac{\hbar^2\pi^2 n^2}{2m^* L_z^2} + \frac{\hbar^2 k_{x,y}^2}{2m^*}, \tag{3.2}$$

where L_z is width of the well, A is the normalization area in x-y plane, m^* is the effective mass.

3.1.1 Intersubband absorption

A subband includes many electrons occupying states with different in-plane momenta, which leads to a Fermi energy depending on 2D quantum well density of states. Unlike intrinsic photoconductors which use interband transitions, QWIPs must be doped to supply the necessary electrons (holes) for absorption to take place in the subband. Quantum wells can be doped either n-type or p-type and barriers are typically undoped, depending on photocarriers being used in detection. In this work, only the conduction band electrons will be considered since the devices studied are n-type.

The absorbed infrared radiation excites electrons (holes) in conduction (valence) band from the doped quantum-well ground state to an unoccupied excited state in the same band. According to position of the energy of excited state, QWIPs are labeled as bound-to-bound (B-B) [57], bound-to-quasibound (B-QB) [58], and bound-to-continuum (B-C) [59], where excited state is within the well, at the edge of well, and outside of the well, respectively. Figure 3.2 shows stylistic representation of a B-B QWIP, a B-QB QWIP and B-C QWIP. The B-B QWIPs and the B-QB QWIPs need higher electric fields for tunneling through the tip of the barrier and contributing to the photocurrent. The spectrum of B-C QWIPs is much broader than that of B-B or that of B-QB QWIPs due to more delocalized excited states in the well. The responsivity of the B-B QWIP is significantly low compared with that of the B-QB and the B-C QWIPs. Because, for an excited electron to reach the continuum in the B-B QWIP in addition to transitions between the states, tunneling is also required. The B-QB QWIPs are preferred due to their high detectivity.

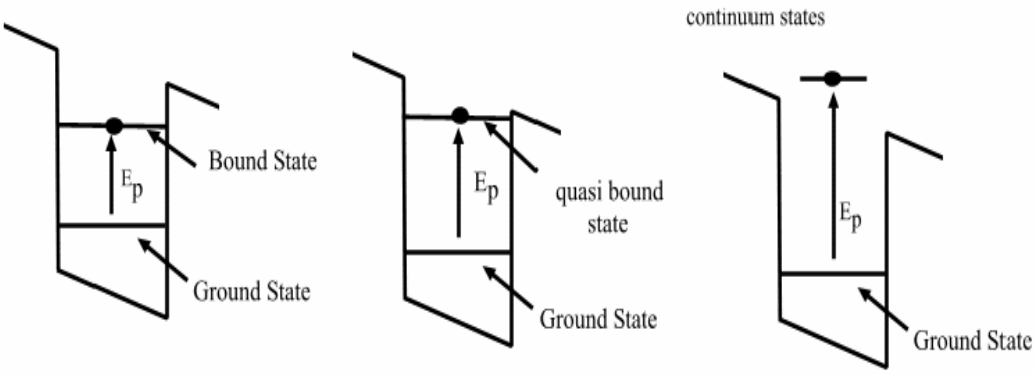

Figure 3.2: Band diagram of a quantum well with bound-to-bound (a), bound-to-quasi bound (b), and bound-to-continuum (c) transitions.

The base current with no illumination is called as dark current, i.e. a noise. The dark current in a multiple-quantum-well photodetector is mostly generated by three mechanisms. These are i.) temperature-independent quantum mechanical sequential tunneling through the barriers between the wells, ii.) thermally assisted quantum mechanical tunneling through the last barrier into continuum states, iii.) classical thermionic emission. The aim is to maximize the ratio of photocurrent to dark current. A unique method of elimination of thermally assisted conduction is the reduction of lattice temperature. Device cooling is required to lessen this thermionic based dark current but this is an added expense and a potential area of malfunction. Sequential resonant tunneling dominates the dark current at very low temperatures, e.g. 30 K or less. This tunneling can be controlled by suitable choice of the barrier thickness such that the probability of tunneling is almost zero, however any further increase in barrier thickness can reduce photocurrent. Doping density affects thermal radiation rate as well as photocurrent rate. The performance of detector is made as high as possible, by optimizing well doping and minimizing the dark current. Therefore, tailoring QW structures with the choice of suitable parameters such as, the depth of the wells, well-doping, widths of the wells and barriers, is important to obtain optimum performance.

Another way of decreasing the dark current due to thermionic emission is to use the B-QB QWIP. Transition to a quasibound state maximizes intersubband absorption and provides excellent electron transport. Furthermore, in the B-QB QWIP the energy barrier to thermionic emission is several meV larger than the case for B-C QWIP. The energy barrier for thermionic emission is the potential height from the ground state to the well edge. In the B-QB design, the first subband is pushed deeper into the well, and this provides the advantage of having higher barrier for thermionic emission when it is compared with that in the B-C QWIP (i.e., $I_d \propto \exp(-\Delta E / kT) \approx \exp(-1)$ for T=70K). In this study, the B-QB QWIP is considered in the Ensemble Monte Carlo simulations.

3.1.2 Light coupling in n-type QWIPs

QWIPs can absorb photons in the subband, only in the case of the incoming light with an electric field component in the growth direction. Then, the electron can be forced to jump to the excited state. As a transverse wave, the electric field component and its propagation direction are perpendicular to each other, so a normal incidence photon is not absorbed. Illuminating the QW structure via 45° polished facet which is illustrated in Figure 3.3.a is an alternative method to overcome the problem in absorption of normal incidence, but it is useful only for single element detectors or linear arrays. For two-dimensional arrays of detectors, a grating which is in shown Figure 3.3.b is a good solution to couple normally incident light to an imaging array of QWIPs. During the fabrication of these detectors, a special rough reflector, a grating, is placed on top and it is illuminated from the back. The roughness (periodic or random) is necessary to change the angle of incidence. Additionally, microlenses are installed to increase absorption of photons by the detector. The microlenses concentrate the incident infrared radiation into a fraction of the area of each pixel. There can be one micro lens for each pixel.

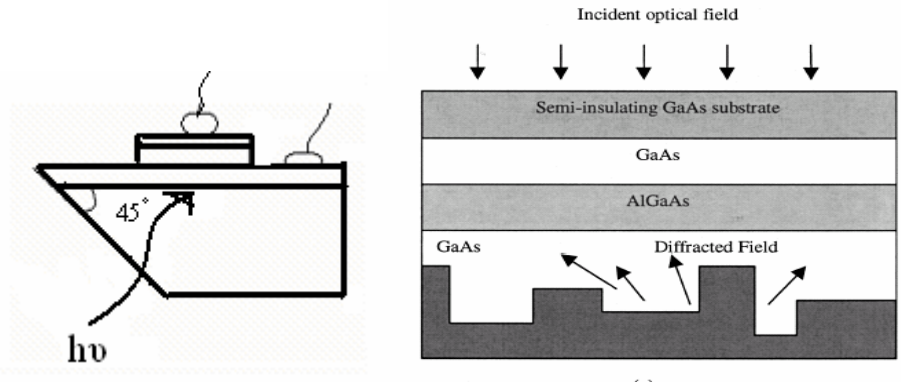

(a) (b)

Figure 3.3: a) The QW structure with a 45° polished facet, b) Grating structure in a QWIP [60].

3.1.3 Low-noise QWIP

QWIPs can operate as a photoconductor or photovoltaic device. In photoconductive QWIPs, an electric field is created perpendicular to the layers via applied bias voltage at the doped contact layers, as shown Figure 3.4.a. QWIPs also operate in photovoltaic mode [61] which gives rise to superior noise properties for large integration times. The photoconduction mechanism of a low-noise QWIP is illustrated in Figure 3.4.b. There are four zones with different functions in a period. In the first zone, called the excitation zone, carriers are optically or thermally excited to quasi bound state and then pass to the drift zone, which is the second zone. Different from the standard QWIP structure there are two additional zones for controlling the relaxation of the excited carriers. Capture zone, the third one, is used for capturing all the continuum electrons via a tall barrier. The last zone of the period is the tunneling zone where the electrons are transmitted to ground state of the subsequent period through the barrier. The advantage of the four-zone QWIP is to be free from generation-recombination noise which is dominant in photoconductive QWIPs. The drawback of this low-noise QWIP is lower gain. In the scope of this study, standard photoconductive QWIP structures are examined in which the major noise source is the G-R noise [61].

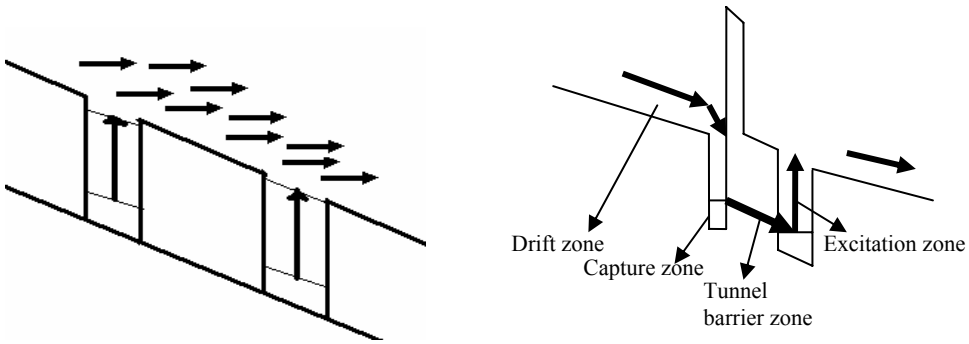

(a) (b)

Figure 3.4: Potential distribution and transport mechanism of a low-noise QWIP a) in photoconductive QWIPs, b) in photovoltaic QWIPs.

In the QWIP technology, n-type doped QWs are widely used due to their advantages over p-type QWIPs. N-Type QWIPs have higher responsivity and detectivity due to higher mobility, higher optical absorption and photoconductive gain with low electron mass compared to p-type QWIPs. Unlike n-type QWIPs where the quantum-mechanical selection rule in the conduction band with the Γ-symmetry forbids normal-incidence absorption, in p-type QWIPs there is a strong mixing between the light and heavy holes in the valence band and this permits normal-incidence absorption [62]. So grating-less FPA is possible in p-type QWIP and this becomes a very important advantage since grating complicates the fabrication process for QWIPs and limits the pixel size.

3.1.4 Multi-color QWIPs

Rapid progress in QWIP technology has made high performance FPA achievable in a short time [63-65]. For highly developed sensing and imaging systems, QWIP technology goes multicolor. Multi-colors detectors can be used for temperature registration, chemical analysis and target identification. For two color detection, a stacked QWIP includes large color separation from the MWIR to LWIR wavebands. Two-color detection is desirable for determination of the absolute temperature of a target, for instance distinguishing a warhead from

decoys. The number of QW stacks depends on the number of color the detector includes. Figure 3.5 illustrates a four-color QWIP. A simplified QWIP structure (S-QWIP) is used by reducing the number of QW's in a QWIP to reduce cost of the MBE growth. S-QWIP's with just three QW's have been shown to have good electron confinement in each QW and the detector provides high performance [66]. The voltage tunability among the stacks must be arranged according to detection wavelength. To detect the LW colors, large bias voltages are needed in a multi-color QWIP.

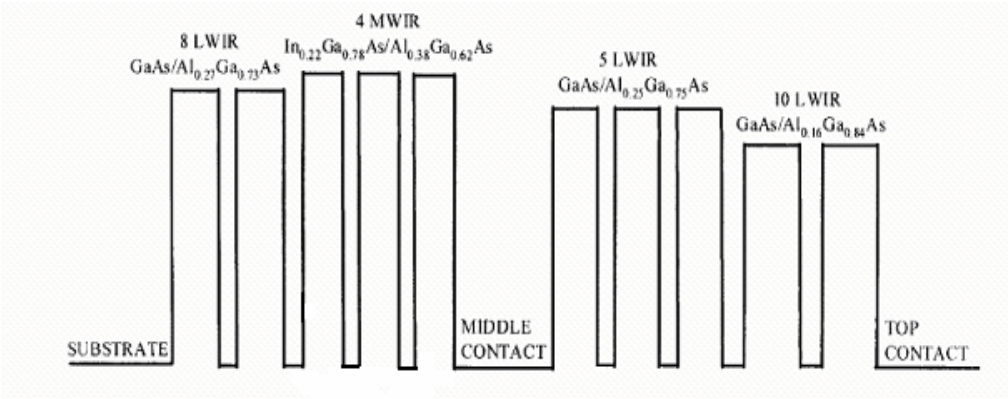

Figure 3.5: The schematic energy band diagram for the four-color QWIP [67].

3. 2 QWIP Focal Plane Fabrication in QWIPs

The growth technologies used in QWIP fabrication are mainly molecular beam epitaxy (MBE) and metalorganic chemical vapor deposition (MOCVD). MBE is developed in the early 1970s as an ultra-high vacuum thin film technology [68]. In an MBE system, a wafer is grown with extremely precise control over layer thickness and doping profile, and high uniformity. MOCVD is also unique and important epitaxial crystal growth technique which yields high quality low dimensional structures for fundamental semiconductor physics and electronic devices [69, 70]. MBE systems are safer than MOCVD since sources of a wafer are dangerous especially in the gas phases and MBE system uses solid sources rather than gaseous ones.

A standard QWIP fabrication involves many technologies and equipment [71]. The fabrication of detector pixels includes the UV-photolithography for sample patterning and etching for the pattern transfer. In the next step, a passivation layer is constructed for neutralizing the surface states and insulating the covered areas. Then, patterning and etching of the passivation layer to produce opening for the metal connection to each detector pixel are needed. An important step is fabrication of indium bumps which form interconnection between the detector and readout-integrated-circuit (ROIC). Next, hybrid coupling (flip-chip bonding) of the detector substrate with a Si-based ROIC is made. Underfill is needed between FPA and ROIC. The underfill supplies the necessary mechanical strength to detector array and readout hybrid, prior to the thinning process. To enhance the optical coupling, the detector substrate is thinned by abrasive polishing or wet etching. Finally, the detector is packaged.

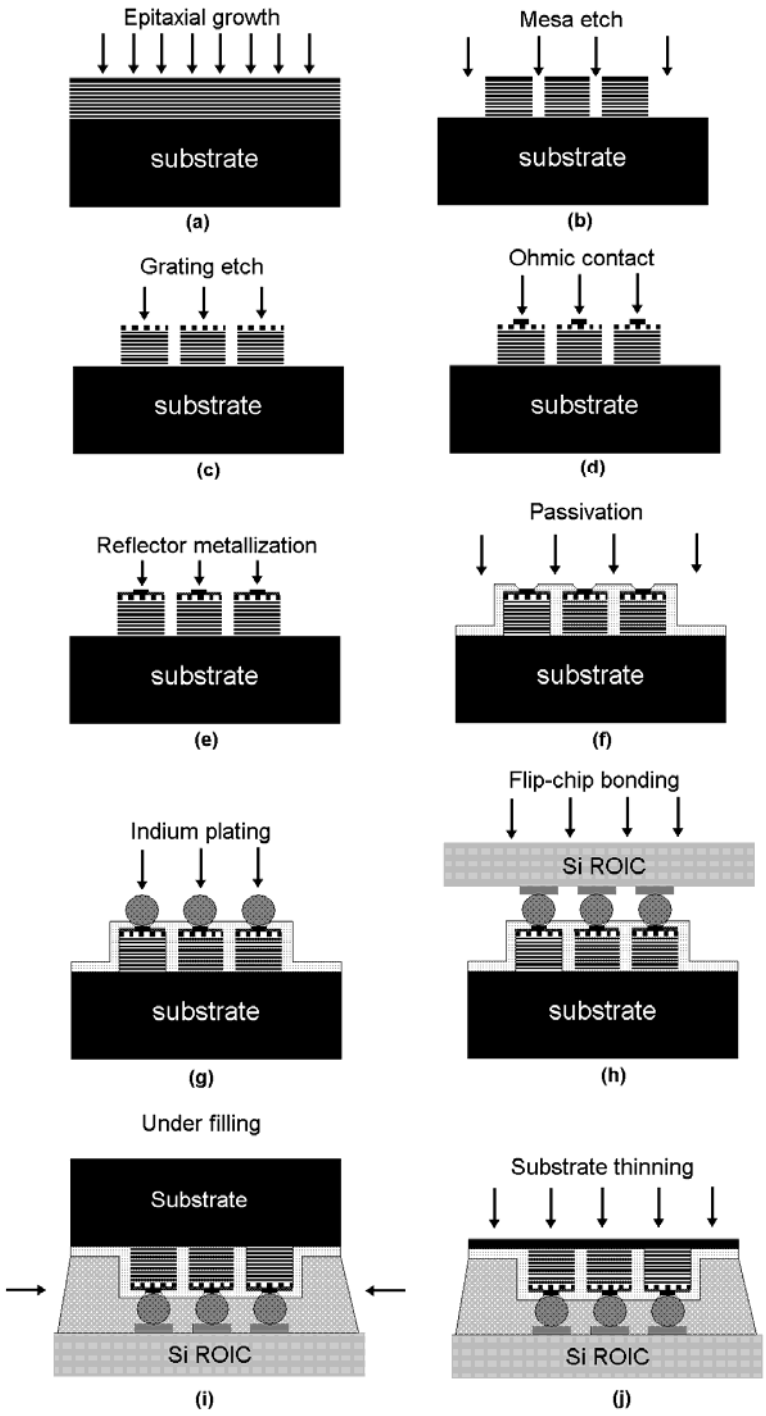

Figure 3.6: Standard QWIP fabrication process steps: (a) Epitaxial growth, (b) mesa etch, (c) grating etch, (d) ohmic contact, (e) reflector metallization, (f) passivation, (g) indium plating, (h) flip chip bonding, (i) under filling, and (j) substrate thinning [72].

3.3 Figure of Merit and Detector Parameters

Figures of merit are used to compare detectors with each other. The main figures of merits for infrared photodetectors are detectivity, noise equivalent temperature difference, responsivity and in the following sub-sections the main parameters of QWIPs are described.

3.3.1 Responsivity

Responsivity is defined as the photocurrent to the incident optical power. It is given by,

$$R = \frac{I_{ph}}{\hbar \omega \Phi} = \frac{\lambda_c}{\hbar c} g \eta \ , \tag{3.3}$$

where λ_c denotes the cut-off wavelength of the detector, η the absorption quantum efficiency, g the photoconductive gain. The quantum efficiency represents how well the detector is coupled to the radiation to be detected. Gain is defined as the number of carriers passing the contact per one generated pair [73].

3.3.2 Detectivity

Detectivity characterizes normalized signal to noise performance. The peak detectivity is defined as [59, 74]

$$D^* = \frac{R\sqrt{A\Delta f}}{i_n}, \tag{3.4}$$

where R stands for the responsivity, A for the pixel area, Δf for the noise bandwidth and i_n for the thermal noise.

3.3.3 Signal to Noise Ratio (SNR) and Noise Equivalent Power (NEP)

Signal to noise ratio (SNR) is not the measure of the detector performance alone due to its linear dependence on radiant power. Noise equivalent power, NEP, is more efficient to measure the detector sensivity which expresses the amount of radiant power that the detector receives to produce a SNR of unity.

3.3.4 Noise Equivalent Temperature Difference (NETD)

The performance of a large imaging array can be determined by noise equivalent temperature difference, NETD, which is the minimum temperature difference when a camera gives SNR of 1. The NETD is given by

$$NE\Delta T = \frac{\sqrt{A\,\Delta f}}{D_B^* \dfrac{dP_B}{dT}}\ , \tag{3.5}$$

where A stands for the pixel area, Δf for the bandwidth, D_B^* for the blackbody detectivity and dP_B/dT for the derivative of the integrated blackbody power with respect to temperature [63, 75, 76].

3.3.5 Capture Probability

The capture probability (p_c) is the fraction of photoelectrons captured in a particular quantum well when the photocurrent is passing through that well [77]. It is given as

$$p_{capture} = \tau_{transit} \ / \tau_{capture}\ , \tag{3.6}$$

where $\tau_{transit}$ stands for the time required for an electron to transit the region where it can be captured and $\tau_{capture}$ stands for the time before recapture when the electron is in this region. The current loss by capturing is accompanied by

the photoemission from the well, i.e., the escape probability is equivalent to the capture probability at a steady state.

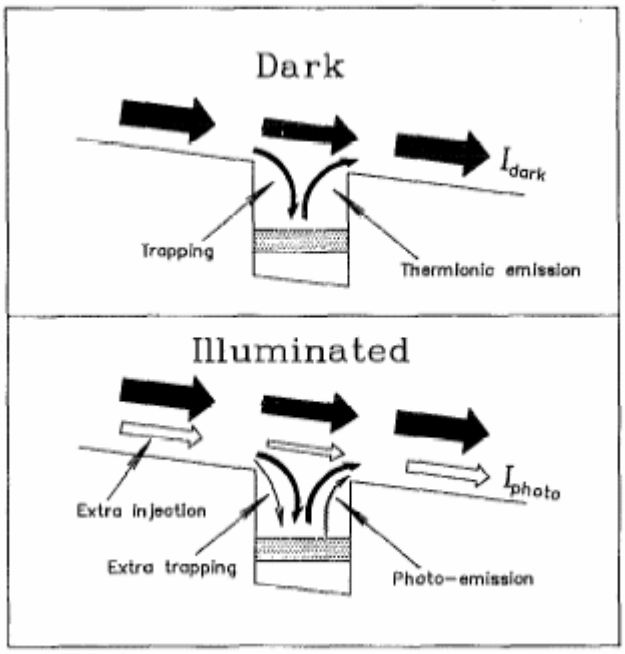

Figure 3.7: The photoconductive gain mechanism [77].

3.3.6 Noise

Noise is an undesired signal observed at the output. There are several noise sources in photodetectors: e.g., it is 1/f noise, Johnson noise, dark current noise, and photon noise. The flicker or the 1/f noise is due to the random trapping and recombination effects involving bandgap states in the device. For GaAs QWIPs, experiments indicate that 1/f noise limits rarely the detector performance. This contribution can be ignored. Johnson noise is inherent to all resistive devices and the noise current is defined as,

$$i_{n,J}^2 = \frac{4k_B T}{R}\Delta f\,, \tag{3.7}$$

where Δf stands for the measured bandwidth and R for the device's differential resistance. In a QWIP, contribution of Johnson noise is usually small [78]. The dark current noise and photon noise usually limit the detector's ultimate performance in QWIPs. The dark current noise is generation – recombination (g-r) in nature. The standard g-r noise is given by [79]

$$i_{n,dark}^2 = 4 g_{noise} I_{dark} \Delta f \,, \tag{3.8}$$

where g_{noise} is the noise gain, and I_{dark} is the device dark current. The g-r noise is dominant in the QWIP operation.

3.4 MCT versus QWIP

In almost 200 years old history of IR, MCT has been developed as good infrared detector technology since 1959 [47, 80] The rapid progress in QWIP is very impressive since 1985 when West and Eglash first observed the infrared absorption in a GaAs/AlGaAs QWIP structure [81]. There are fundamental advantages and limitations of materials when the MCT and the QWIP structures are compared.

MCT has a very high quantum efficiency and detectivity. The reported quantum efficiency is larger than %70 and the detectivity is around 10^{12}cmHz$^{1/2}$W^{-1}. However, in FPA fabrication of MCT, some difficulties are arising, especially in growth and device stability. The problems can be listed as follows: First, material defects can cause low R_0A for some VLWIR pixels. Second, it is hard to manage the stability of alloy and to control material growth. Third, MCT array can be damaged under high radiation due to narrow bandgap and defects in material. The important drawback of MCT FPA is low yield and high costs compared with QWIP FPA. For example, with 10 μm peak wavelength, MCT FPA and QWIP FPA, the ratio of their costs per inch is 10/1 but ratio of their

yields 1/2. [82]. Next, reproducibility of MCT detectors is poor since the sensitivity of bandgap to composition is high.

QWIPs have been demonstrated to have competitive detectivity and the promise of focal play array. Point-to-point comparison favored MCT detectors with higher detectivity [83]. QWIP superiority in focal play array applications has been reported by various groups [84, 85].

Using the QWIP as a detector has many advantages over the traditional HgCdTe [71]. In QWIP fabrication, mature III-V growth technology is used. Common III-V materials, GaAs and InP which are used in QWIP fabrication were developed previously in lasers, LEDs and microwave circuitry. Using $GaAs/Al_xGa_{1-x}As$ instead of mercury cadmium telluride has crucial advantages. These materials are considerably less expensive and are more uniformly grown than MCT. Moreover, monolithic integration of GaAs wafers with high-speed GaAs multiplexers and other electronics has advantage on manufacturing cost with existing infrastructure. QWIPs are good at radiation-hard applications due to their relatively large band-gap. The challenging point of QWIPs is their excellent array uniformity and possibility of multi-color arrays. Their photoresponse spectrum is narrow and, it is desirable due to low spectral crosstalk for multicolor applications. Another advantage of QWIPs is their high R_0A value which allows long integration time or more image accumulation.

QWIPs are usually used in thermal imaging applications but they are also suitable for ultra-high frequency applications due to their fast response. Some of high frequency applications of QWIPs are remote sensing of atmospheric molecular species, CO_2 and quantum cascade laser-based communications and infrared notch filters for the 3-5 μm spectral window. For high frequency applications, the most important parameter is absorption which can be adjusted by doping and a high dark current is tolerable due to strong input signal which is often a laser source. A disadvantage of n-type QWIPs is the required light

couplings. Requiring lower sensor temperature than MCT for 3-5 μm and 8-12 μm windows is another drawback of QWIP.

3.5 Applications of QWIP

The QWIP detectors have many applications in military, commercial and scientific research, offering improved temperature sensitivity. Some applications are given below.

The health care industry: A tumor is basically the uncontrolled proliferation of cells. During growing of tissue, there is a high metabolic activity going on and the tumor tissue needs more blood supply. So the surface of a tumor is warmer than the interior regions. A QWIP camera with high thermal and optical resolution can be used in diagnosis of a tumor. For example, the QWIP camera for surgical applications can be used to distinguish between normal cells and brain tumor cells. The National Aeronautics and Space Administration's (NASA) Jet Propulsion Lab (JPL) has been working on this camera. Noninvasive detection of breast and skin cancer is possible with QWIP cameras [3].

Fire fighting: The infrared imaging enables us to see through dust and smoke [86]. So QWIPs have important applications in fire-fighting. Fire-fighters and helicopter camera crews can use the QWIP camera to see forest fire hot spots from the air through heavy smoke.

Astronomy: Infrared technology is also utilized in space program [86]. The cameras can detect the infrared through dust clouds and image deep into dusty star-forming regions where visible sensor cannot penetrate. They are also used to search for cold objects such as planets orbiting nearby star.

Military Applications: The military applications of infrared detection include night vision, rifle sight, military surveillance, guidance and tracking for missiles as well as for interceptors [86]. For space-based surveillance sensors, LWIR and VLWIR are suitable wavelength bands to detect targets which are mostly cool with low background irradiance level. For tactical military applications, the detection bands are NIR, MWIR and LWIR which are determined by the atmospheric transmission windows. So high resolution, large area infra red FPAs in 3-5 μm and 8-12 μm windows with high sensitivity, high uniformity and stability are needed.

The QWIP technology also has many potential uses for search and rescue, detecting faulty welds and blockages, and volcano observation.

CHAPTER 4

ENSEMBLE MONTE CARLO MODELLING OF QUANTUM WELL INFRARED PHOTODETECTORS

Monte Carlo (MC) device modeling technique is a statistical method based on the simulation of the particle motion in the device at a microscopic level. In MC, the process is to simulate the motion of individual particles under the influence of an electric field and some random scattering forces. Modeling physical problems with MC methods enables us to examine complex systems. The interactions between two atoms can easily be solved whereas exact solution of the interactions for hundreds or thousands of atoms is unachievable with analytical methods. A large system can be sampled in a number of random configurations, and data can be used to describe the complete system. Increasing availability of powerful computers means that the complexity with which physical systems can be modeled is increasing.

Although QWIP is a unipolar photoconductor which has a quite simple layer structure, precise QWIP modeling is actually a difficult task. A QWIP is a very complicated problem with many electrons. In this problem, the transport of the

continuum electrons which are far from equilibrium conditions need sophisticated models including reflection of electrons at the quantum well (QW) locations. An accurate description of the capture and emission mechanisms requires a realistic calculation of the related scattering rates.

There have been many studies on analytical modeling of QWIPs, as well as numerical modeling based on the drift-diffusion model of electron transport [14-16, 77, 85, 87-92]. However, the well-known limitations of the drift-diffusion model may cause unreliable results in a QWIP structure [19]. In this model, the carrier velocity is an instantaneous function of the electric field, neglecting carrier velocity overshoot behavior and hot electron effects. The well-known alternative methods are hydrodynamic transport models and MC modeling.

In the hydrodynamic transport models, all the valleys are considered and their results are more reliable than the drift-diffusion formulation for the simulation of semiconductor devices, but the application of this method to QWIPs is not simple. In this approach, the energy dependent parameters are obtained from MC simulations on bulk material. For multi quantum well (MQW) structure, extraction of these parameters is much more complicated, since vertical transport in a MQW structure is considerably different than that for the bulk material.

EMC simulation is a suitable tool for investigation of QWIP operation and characteristics. The aim is to optimize the device parameters for better performance by minimizing the expensive experimental optimization procedure. There are several groups working on simulation of QWIPs [19, 23-31]. These studies investigate various important features of QWIP operation. In the scope of this work, we search for answers to unexplained features in QWIP's operations with detailed EMC simulations. The EMC simulation code used in this study was mostly developed by O. O. Cellek[33, 34 and 35].

4.1 Wavefunction Calculation

Wavefunctions are found by solving the effective mass equation. Wavefunction calculations in this EMC program are developed by O. O. Cellek and U. Bostancı. The effective mass equation for the envelope wavefunction of subband n is

$$-\frac{\hbar^2}{2m^*}\frac{d^2 f_n(z)}{dz^2} + V(z) f_n(z) = E_n f_n(z), \tag{4.1}$$

where V(z) is the effective potential [93].

In the numerical procedure, the structure is divided into small mesh cells, length of which is Δx. Then the wavefunction and the potential energy for i'th cell is expressed as

$$f(z) = u_i, \quad V(z) = V_i \quad . \tag{4.2}$$

The initial conditions are

$$\begin{aligned} f(0) &= 0, \quad \frac{\partial}{\partial z} f(0) = 0, \\ f(L) &= 0, \quad \frac{\partial}{\partial z} f(0) = 0. \end{aligned} \tag{4.3}$$

The effective mass equation is rewritten in terms of eigenvector of u;

$$H f = \frac{\hbar^2}{2m}\frac{(-u_{i+1} + 2u_i - u_{i-1})}{\Delta x^2} + V_i u_i . \tag{4.4}$$

This is an eigenvalue equation,

$$Hu_i = E u_i, \tag{4.5}$$

where the H matrix is given as

$$\begin{bmatrix} 2+V_1 & -1 & 0 & . & . & . \\ -1 & 2+V_2 & -1 & 0 & . & . \\ 0 & -1 & 2+V_3 & -1 & 0 & . \\ . & 0 & -1 & 2+V_4 & -1 & 0 \\ . & . & . & . & . & . \\ . & . & . & . & . & . \end{bmatrix}_{m*m},$$

here m denotes the number of mesh (point cell) in the structure. The mesh length is taken as 1 Å. The length of each barrier region is taken as 1000 Å and the well length is taken 36 Å or 44 Å. The H matrix is solved by using a package program in Fortran-90.

Electric field and electrostatic potential are found for each well by using the Poisson's equation in a quantum well which is expressed as

$$\frac{d^2U(z)}{dz^2} = \frac{e}{\varepsilon}\left[\sum_{i=1}^{m} n_i \left|\psi_i(z)\right|^2 - N_D(z) + N_A(z)\right], \tag{4.6}$$

where m indicates number of subbands, U(z) is the electrostatic potential, $N_A(z)$ is the ionized acceptor density, $N_D(z)$ is the ionized donor density, and n_i is the density of electrons in subband i which is given as,

$$n_i = \frac{m^* kT}{\pi\hbar^2} \ln\left[1 + \exp\left(\frac{E_F - E_i}{kT}\right)\right]. \tag{4.7}$$

Coupling of the effective mass equation with the Poisson equation gives the complete solution of wavefunctions and the bound energy levels so equations (4.1), (4.6) and (4.7) are solved self consistently and an iteration number is

chosen large enough to give correct results. The wavefunctions are calculated only once at the beginning of the simulation because of extreme time consumption [94].

4.2 Potential and Electric Field Calculation

The potential distribution is found from solution of the one dimensional Poisson equation. Then, the electric field distribution is obtained from the potential distribution. The cloud in the cell (CIC) method is used for determination of charge density. The principle of the CIC method is to share the electron charge with the surrounding mesh cells which is taken as 4 Å [95]. Each electron has the cell like shape. If an electron is only located at the centre of cell, its charge is assigned to that cell, otherwise, the area occupied by an electron in the cell gives the charge contribution of the electron to that cell. An example of this distribution is given in Figure 4.1.

The Poisson equation is given as

$$\frac{d^2}{dz^2}U = -\frac{q}{\varepsilon\, h_z}(N_{ds} - n_s), \tag{4.8}$$

where U stands for the electrostatic potential, N_{ds} for the sheet density of related mesh and L_z for the mesh length in z dimension. After discretization, the Poisson's equation is rewritten as

$$\frac{U_{i-1} - 2U_i + U_{i+1}}{h_z^2} = -\frac{q}{\varepsilon\, h_z}\big(N_{ds} - n_s(i)\big), \tag{4.9}$$

where $n_s(i)$ is electron sheet density which is found by the CIC method of mesh i. The electric field is found by solving the equation

$$E = -\nabla U \,. \tag{4.10}$$

The Poisson's equation should be solved in sufficiently small time intervals to track the motion of the electrons accurately. In our simulations the Poisson equation is solved in every 20 fs and the electric field distribution is so updated.

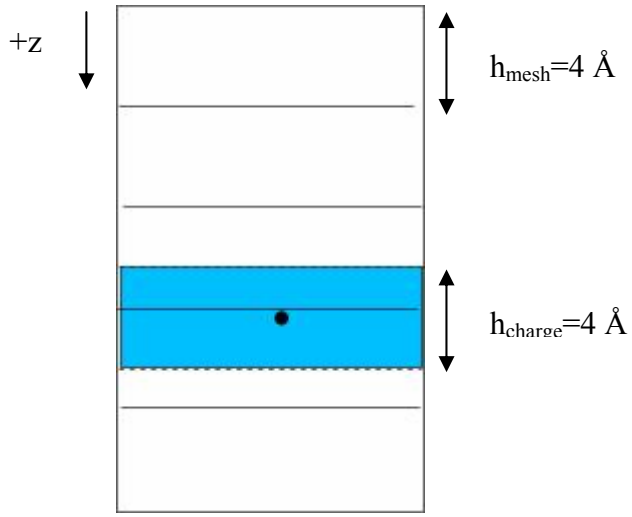

Figure 4.1: Illustration of the CIC method

4.3 Scattering Rates

In order to obtain correct results in determining the QWIP behavior, realistic modeling of capture and emission mechanisms is required. Both 3D and 2D electrons are simulated by taking size quantization into account in Γ and L valleys of the conduction band. The rates of the necessary 2D↔2D and 2D↔3D scattering processes are also evaluated. Scattering rates are also calculated only once at the beginning of the simulation for each electron energy [94].

The most relevant scattering mechanisms included in the simulation are polar optical phonon (POP), acoustic phonon, ionized impurity, alloy, and intervalley

(equivalent and non-equivalent) scatterings. Electron-electron scattering which will presumably be important at higher QW electron concentrations is ignored due to the low electron concentration. The EMC simulator developed in this work simulates both 3D and 2D electrons considering size quantization in both Γ- and L-valleys of the conduction band. $Al_xGa_{1-x}As$ with x~0.3 is mostly used as the barrier material in long wavelength infrared (LWIR) QWIPs. A significant amount of the barrier electrons is in the L-valley under typical bias voltages since the small enough energy spacing allows easy scattering between the central and satellite valleys in $Al_xGa_{1-x}As$ with x~0.3. Moreover, POP emission rate in this valley is higher than that in Γ valley. The continuum electrons in the Γ-valley have higher kinetic energy due to faster heating during their transport in the barriers which is one of the reasons of lower capture probability in the Γ-valley. As a result, electron capture through the L-valley QW (L-QW) may significantly affect the characteristics of the QWIPs with the considered barrier composition.

Our simulations revealed the dominance of electron capture through L-valley which is shown by tracking the electrons which reach the GaAs well regions [34, 35]. Considering the origin of captured electrons, it is observed that the percentage of the electrons entering the GaAs well regions in L-valley that are eventually captured in Γ-valley QW may be an order of magnitude larger than that of the electrons entering the well regions in Γ-valley under typical bias voltages in the $Al_{0.3}Ga_{0.7}As$/GaAs QWIP structure [34]. The first step in the capturing of these L-valley originated electrons is the transition to the L-valley QW by 3D→2D POP emission. Then, they are scattered to the Γ_{2D} state where they quickly lose energy by intra-subband phonon emission, and are eventually captured in the Γ-QW. Reasonably precise evaluation of the scattering rates between the states in the central and satellite valleys of the conduction band is necessary for accurate simulation of the capture mechanism.

In this work, the transitions of the electrons between the continuum and bound states ($\Gamma_{3D} \leftrightarrow \Gamma_{2D}$ and $L_{3D} \leftrightarrow L_{2D}$) are modeled as 3D↔2D POP scattering path following the approach of Khalil *et al.*[96]. The 2D↔2D, and 3D↔2D scattering rates are calculated using the solutions of the effective mass equation.

The 2D↔2D and 3D↔2D intervalley scattering rates between Γ and the higher energy valleys are calculated by using the approach of Educato *et al.* [97] and Goodnick and Lugli [98]. Dielectric screening effects are included in the calculation of 2D POP scattering rates [99]. Electron tunneling through the emitter contact and the X-valley barrier in GaAs layers, and the quantum mechanical reflection/transmission of electrons by the heterointerfaces are also considered in the simulation [100, 101].

4.4 Intersubband Transition Rate Due to Photon Absorption

In the program, the photoexcitation rate is taken as 10^{10} s^{-1}. Simulation of QWIP with MC technique under low photoexcitation rates is impractical since large amount of computer time is needed to reach steady-state. Under the selected photoextitation rate, the simulation reaches steady state in several nanoseconds beyond which, no significant change occurs in the observed quantities. In this selected photoexcitation rate, barrier electron density is low enough and the E-field distribution is not affected. This rate is also small enough to avoid saturation of intersubband absorption. Under such a photoexcitation rate, the E-field in the main body of QWIP may be smaller than that under near-dark conditions due to larger voltage drop near the emitter contact [101].

4.5 Simulation Procedure

One dimensional ensemble Monte Carlo simulation is performed after pre-calculations. Pre-calculations include calculation of the wave-functions and of scattering rates. These are written to look up tables at the beginning of the program. To make the program applicable easily to different conditions,

necessary parameters are given in the input files. The flow charts of the program are illustrated in Figures 4.2 and 4.3.

First, all variables are initialized and all input files and stored results of pre-calculation is read. Next, all the electrons are uniformly distributed throughout the structure. Then the main loop starts and it can be stopped after around 10 ns at which point the device reaches the steady state and this is large enough time interval for averaging output data. In the main loop, each particle is handled separately and both momentum and position in real space are tracked within 1fs time interval. This time interval is taken small enough to obtain high accuracy such that an electron can not drift more than one mesh. After simulating all electrons, at the beginning of next cycle, charge neutrality is satisfied. CIC method is used for charge distribution throughout the device.

All the detailed results can be obtained at the end of program such as populations and the energy distributions in each valley (Γ, L and X), charge distribution in subbands, current density at contact and local current on the barriers, the potential and the electric field distribution throughout the device, the frequency of scattering rates etc.

The simulation programs also present the progress of simulation on the computer screen. Particles are shown according to their position and energy. One selected carrier can be traced closely on the screen which also includes scattering events and reflections. A snapshot of the program is given in Figure 4.4.

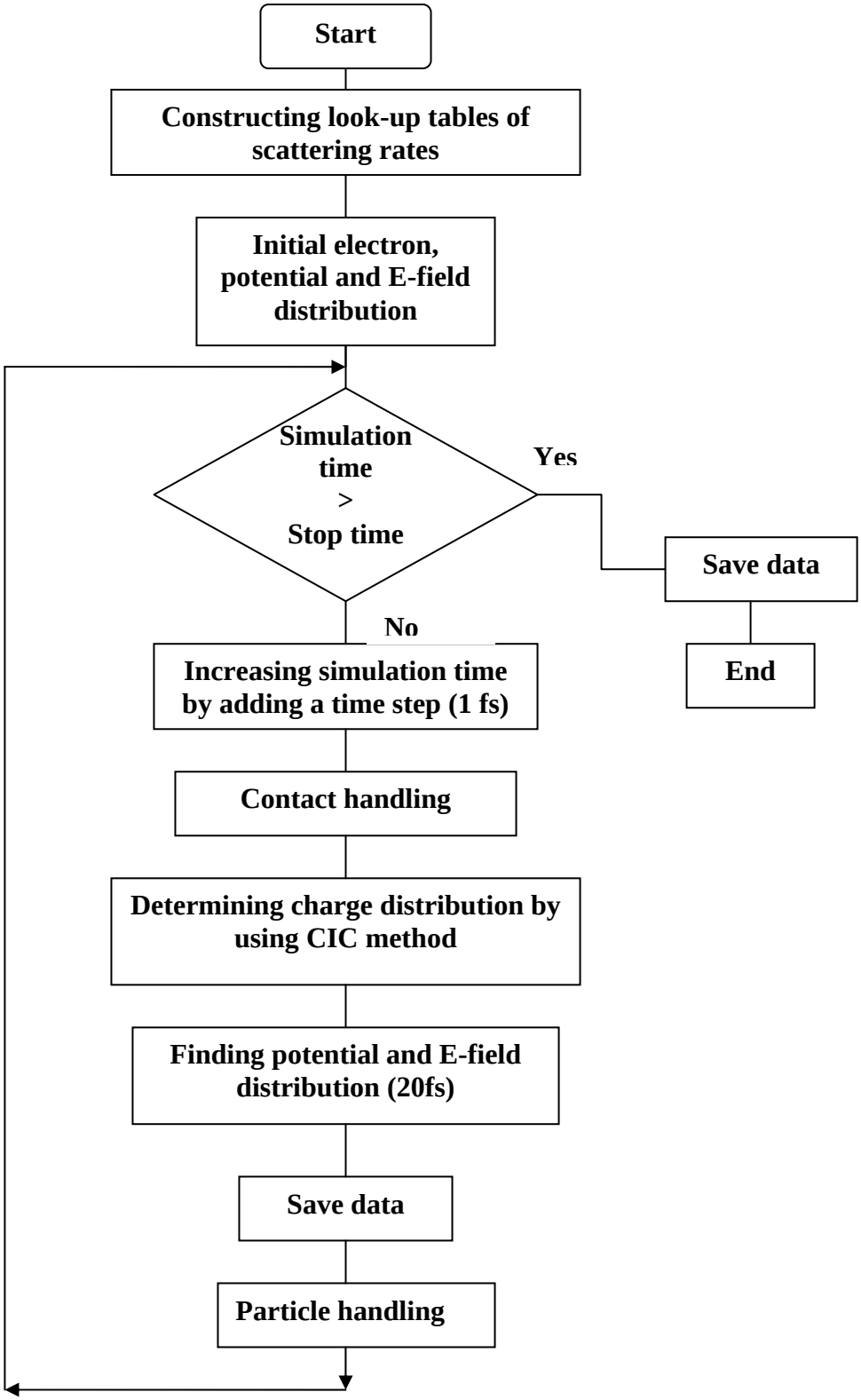

Figure 4.2: Flow Chart of our Ensemble Monte Carlo Simulation.

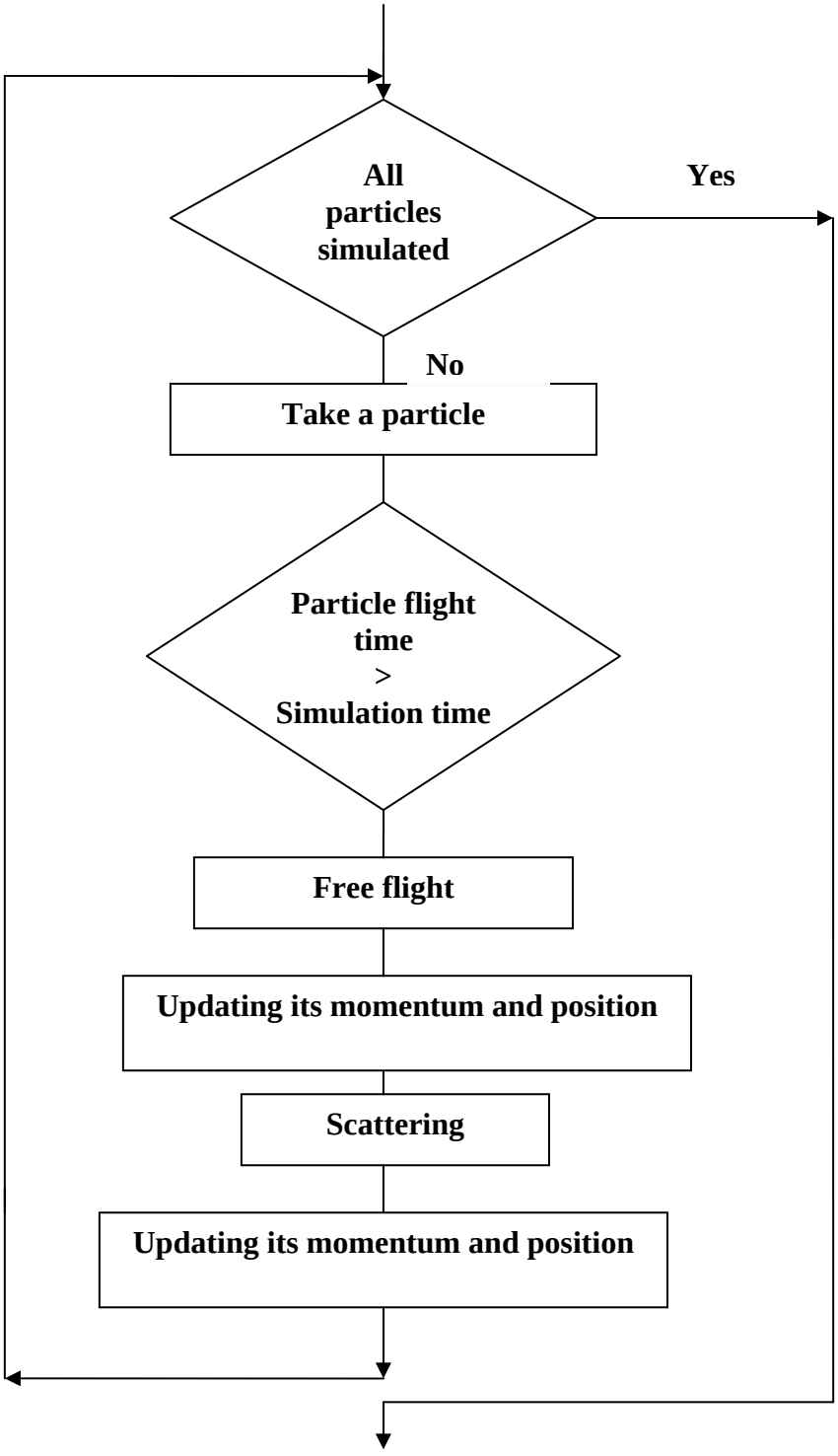

Figure 4.3: Flow Chart of particle handling section.

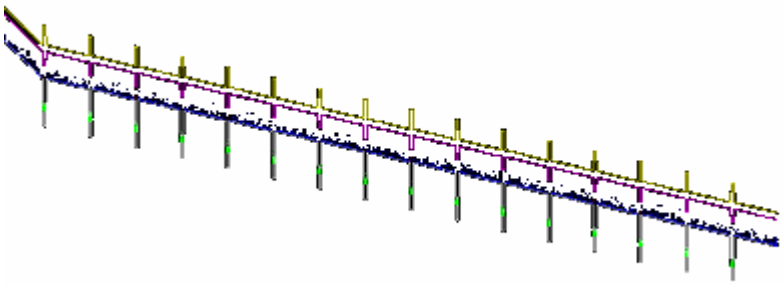

Figure 4.4: A snapshot from our simulation. The bottoms of Γ, L and X valleys are shown in black, purple and yellow, respectively and electrons in each valley is illustrated with different colour.

4.5.1 Initial and Boundary Conditions

The simulation of actual number of electrons is not possible due to computer capacity and long calculation time. Super charge is used instead of an electron and a super charge includes 4×10^8 electrons in our simulations. There are approximately 2000 super charges or particle in the device at any instant. Device is divided into small meshes and length of each mesh is taken as 4 Å throughout calculations. The carriers are put into meshes according to doping level of the regions. The carriers in the barrier and contact regions are put into Γ-valley and in the well regions; they are distributed into ground state at the beginning of program. Carriers are always injected as Γ-valley electrons at the emitter throughout the simulation time. The initial kinetic energy of the electrons is chosen to be the average thermal electron energy. The initial kinetic energy of the continuum electrons are assigned as

$$E = -\frac{3}{2}kT\ln(r)\,, \tag{4.11}$$

where k is the Boltzmann constant, T is the temperature, and r is a random number which is between zero and one. Initially, the contact potential is set to

the bias potential and the electric field is uniformly distributed through the device.

4.5.2 Interface Treatment at the Band Edge Discontinuities

In AlGaAs/ GaAs QWIPs, the heterojunctions create wells in Γ and L valleys as well as a barrier on X-valley in the GaAs region. The heterojunctions are taken as energy steps in the growth direction, z. When the electron energy is smaller than the energy of discontinuity, it is reflected with reversal of the direction of momentum along z-direction. In case the electrons have larger energy than this potential barrier, the transmission probability is calculated [33]. The process is illustrated in Figure 4.5.

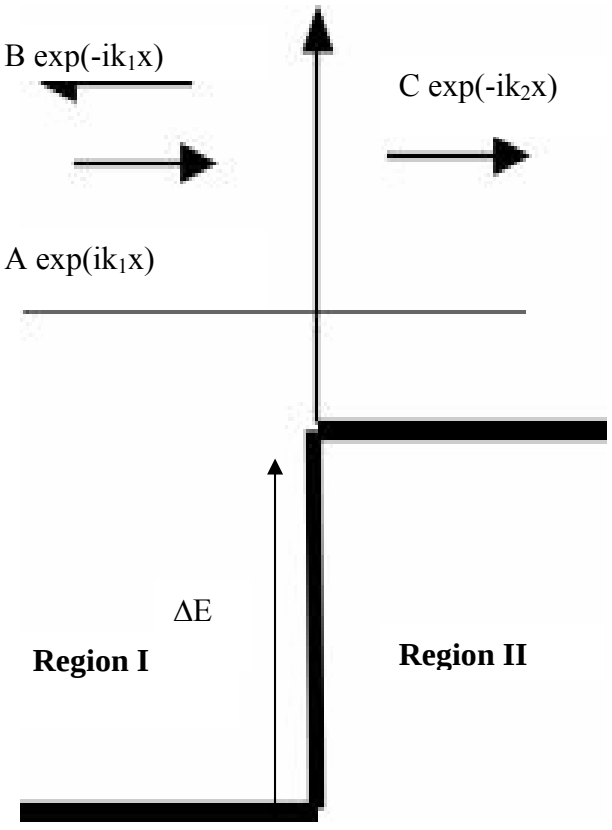

Figure 4.5: Transmission in the heterojunction.

The transmission coefficient is given as [102]

$$T = \left| \frac{J_{trans}}{J_{inc}} \right| = \frac{4 \, k_2 / k_1 \; m_1 / m_2}{(1 + k_2 / k_1)^2} . \tag{4.12}$$

Then, the transmission is checked randomly.

The energy updates are as follows

$$\begin{aligned} E_{well} &= E_{barrier} + \Delta E_c , \\ E_{well} &= E_{barrier} + \Delta E_{c,L} , \\ E_{well} &= E_{barrier} + \Delta E_{c,X} , \end{aligned} \tag{4.13}$$

where E stands for the carrier in well and on the barrier regions and ΔE_c, $\Delta E_{c,L}$ and $\Delta E_{c,X}$ for the conduction band discontinuities of the valleys of Γ, L and X, respectively. In the momentum update only the change in energy affects the momentum component of electrons in z-direction and other components are not changed. The total momentum for entire system (electron gas and crystal), is conserved by z- component transfer between the crystal lattice and electrons [101]

The tunneling of electrons into the X-valley is treated by WKB approximation [101, 33]. The electrons tunnel through the barrier with same energy and momentum. The tunneling probability is given by

$$\begin{aligned} T &\cong \exp(-2 \int_{z_1}^{z_2} \left| \; (z) \right| dz), \\ (z) &= \sqrt{2m^* (\Delta E_{c,X} - KE)} / \hbar, \end{aligned} \tag{4.14}$$

where z_1 and z_2 are the initial and final position of tunneling electron, $\Delta E_{c,X}$ is the energy barrier on X-valley and KE is kinetic energy due to momentum in the growth direction.

4.5.3 Simulation of Carrier Motion

Each carrier is simulated separately. Motion of carriers mainly consists of free flight by the drift and scattering. The duration of the carrier free flights and the scattering events and some reflections are determined stochastically. The simulation is therefore made by generating a sequence of random numbers as shown in flowchart in Figure 4.3. After free flight and scattering, electron's momentum, position and energy are updated.

The flight time can be assigned by using a random number, r, which is given as

$$\tau = -\frac{1}{\Gamma}\ln(r). \tag{4.15}$$

The constant Γ is chosen to be larger than the largest value of the total scattering rate. Γ is taken small enough to minimize the number of self-scattering events. After determination of the time of free flight, the next step is the drift process.

In the drift process in a semiconductor, electrons are regarded as free particles with an effective mass. A semi-classical approach is used. Based on the equations of motion for electrons, the change in the wave vector during the flight time τ is found by integrating the equation of motion with respect to time; thus,

$$\Delta = -\frac{1}{\hbar}\int_{t}^{t+\tau} \nabla H dt' , \tag{4.16}$$

where H stands for the Hamiltonian of an electron with a charge q given by

$$H = E \quad + qV(\ ). \tag{4.17}$$

Under uniform electric field the change in the wave vector is,

$$\Delta \quad = -\frac{q}{\hbar} \quad \tau\ . \tag{4.18}$$

After the carrier is drifted by the electric field, its momentum, position and energy are updated. The following step is a scattering process.

In the scattering process, a normalized distribution of scattering rates is obtained according to the energy of the simulated carrier. This distribution also includes self scattering which is the difference between chosen total scattering rate and the sum of the calculated scattering rates.

This distribution is obtained by using functions $\mathrm{A}_n(E\ )$ defined as

$$\mathrm{A}_n(\quad) = \frac{\sum_{i=1}^{n} \lambda_i(\ )}{\Gamma} \qquad n = 1, 2, ..., N \tag{4.19a}$$

$$\Gamma = \sum_{i=1}^{N} \lambda_i(\ ), \tag{4.19b}$$

where Γ stands for the total scattering rate, N for the total number of scattering mechanisms, and $\lambda_i(\mathbf{k})$ for the scattering rate of i-th mechanism. The schematic diagram of the scattering distribution is given in Figure 4.6. A random number lying between 0 and 1 choose the type of scattering in this distribution by the condition

$$\mathrm{A}_{n-1}(E\ ) < r < \mathrm{A}_n(E\ ) \qquad n = 1, 2, ..., N\ . \tag{4.20}$$

After scattering of the carrier, momentum of this carrier is updated. The scattering rates and momentum updates are described in the appendix.

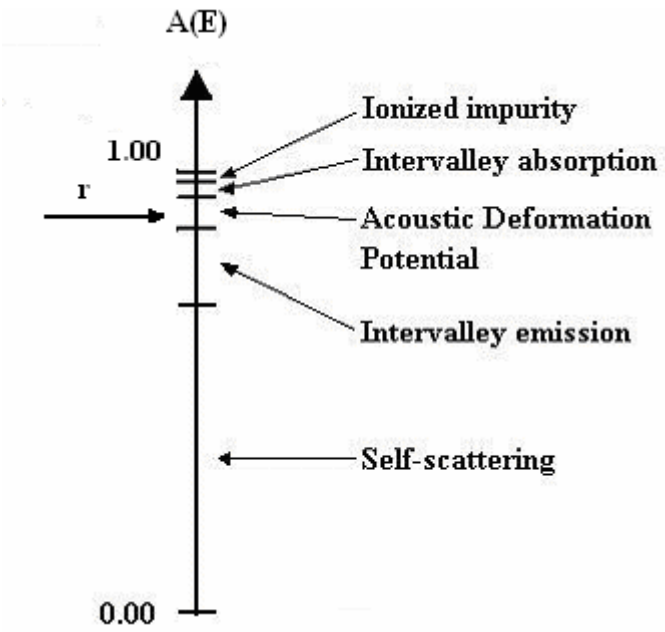

Figure 4.6: Illustration of scattering probability distribution on a line.

4.5.4 Data Collection

Valley occupancies, average velocity and average energy are calculated at the end of program. The occupancy ratios of the electrons on each valley (R_Γ, R_L and R_X) are determined by taking the ratio of the total free flight time in that valley and the total free flight in the cell.

The mean values of velocity and energy can be calculated directly by monitoring each electron flight and taking an average over all flights. The mean carrier velocity during flight time τ can be written as

$$\langle v \rangle_\tau = \frac{1}{\hbar}\frac{\Delta E}{\Delta}, \tag{4.21}$$

where ΔE and Δ are small increments of the carrier energy and wave vector during τ, respectively. According to (4.18), the increment of electron wave vector under a constant electric field is given by

$$\Delta \quad = -\frac{q}{\hbar} \quad \tau \,. \tag{4.22}$$

Substituting (4.22) into (4.21), we obtain

$$\langle v \rangle_{\tau} = -\frac{\Delta E}{e \quad \tau} \,. \tag{4.23}$$

Making use of the mean carrier velocity during τ given by (4.23), the mean carrier velocity during the total simulation time T is calculated as

$$\begin{aligned} \langle v \rangle_{T} &= \frac{1}{T} \sum \langle v \rangle_{\tau} \tau \,, \\ &= \frac{1}{e \quad T} \sum (E_f - E_i) \,, \end{aligned} \tag{4.24}$$

where E_i and E_f stand for the carrier energy at the start of the electron flight and the end of the flight. The summation has to be made for all free flights. The energy increment during each free flight is accumulated to determine the mean carrier velocity. The average electron velocity in a cell is found as

$$v = v_{\Gamma} R_{\Gamma} + v_L R_L + v_X R_X \,. \tag{4.25}$$

The mean carrier energy $\langle E \rangle_{T}$ is calculated as

$$\langle E \rangle_{T} = \frac{1}{T} \sum \langle E \rangle_{\tau} \tau \,. \tag{4.26}$$

Finally, the average electron energy in a cell is found as

$$E = E_{\Gamma} R_{\Gamma} + E_L R_L + E_X R_X \,. \tag{4.27}$$

CHAPTER 5

RESULTS AND DISCUSSION

In this work, we performed the MC simulation of electrical transport in 16-well $Al_{0.3}Ga_{0.7}As$/GaAs QWIPs in the standard structures where well lengths of 44 and 36 Å are chosen. We also let the height of L-QW vary artificially in the $Al_{0.3}Ga_{0.7}As$/GaAs QWIPs. The simulated structure with x=0.3 has sixteen GaAs wells sandwiched between 500 Å thick $Al_{0.3}Ga_{0.7}As$ barriers. The QW n-type doping density is selected to be $1.76x10^{11}$ cm^{-2} in all QWIPs [103]. Material and heterostructure parameters are taken from several sources [104-106], and band nonparabolicities are also included. The details of the energy band diagram are given in Figure 5.1.

In addition to the well length and L-QW height, effects of various parameters on QWIP characteristics are also investigated [35]. In this scope, the QWIP structure with 0.15 Al mole fraction and the simulation of $Al_{0.3}Ga_{0.7}As$/GaAs QWIP with different barrier electron effective mass and energy spacings between the central and satellite valleys is done [35]. The effective mass is reduced by 50% in the conduction band valleys. The energy separation between Γ and L valley is increased to be equal to those in InP.

The first section is devoted to $Al_{0.3}Ga_{0.7}As$ /GaAs QWIPs. In the second section, the capturing mechanism is investigated in various QWIP structures. The charge densities in wells and the electric field distributions in these structures are discussed in section 3. Finally, the gain, the average electron velocity and the lifetime characteristics are given.

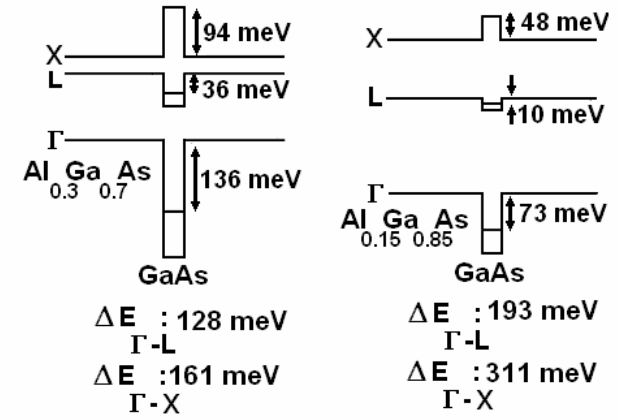

Figure 5.1: The energy band diagrams of $Al_{0.3}Ga_{0.7}As$/GaAs and $Al_{0.15}Ga_{0.85}As$/GaAs QWIP structure [35].

5.1 $Al_{0.3}Ga_{0.7}As$/GaAs QWIP

$Al_xGa_{1-x}As$/GaAs with ~0.3 mole fraction is one of the basic material systems used for IR detection in LWIR range (8-12 μm). In this section, the results of EMC simulation of $Al_{0.3}Ga_{0.7}As$/GaAs QWIP are discussed. The steady-state QWIP characteristics are considered under continuous illumination. The structure consists of 16 wells; length of each is 44 Å and barrier length is taken as 500 Å. The peak responsivity wavelength is expected to be at 8.4 μm [103]. The doping density is taken as 4×10^{17} cm^{-3} [107].

The gain, an important figure of merit, which determines the QWIP's performance, can be expressed as L_d/L where L_d denotes the drift distance of the excited electrons, and L is total device length. There is negative differential

change (NDC) in the gain as seen in Figure 5.2. Levine *et al.* [108] and Schneider *et al.* [109] report strong NDC in the gain of 50-well $Al_{0.26}Ga_{0.74}As$/GaAs QWIPs. This NDC is attributed to ground state tunneling by Levine *et al.* [108], whereas it is explained as the degradation of intervalley transport properties by intervalley transfer in the barriers by Schneider *et al*. [109]. The ground state tunneling is not considered in our simulator so the NDC in the calculated gain can be explained by another reason. Unlike general belief, which relates gain saturation with velocity saturation, gain peaks well before the average electron velocity peak as illustrated in Figure 5.2.

Gain starts to increase with bias under large biases (above ~3 V). Experimental results which are obtained through noise measurements have shown similar behavior [110-112]. It is attributed to avalanche multiplication [110-112]. Avalanche multiplication is not included in the simulator; therefore another factor can also be considered.

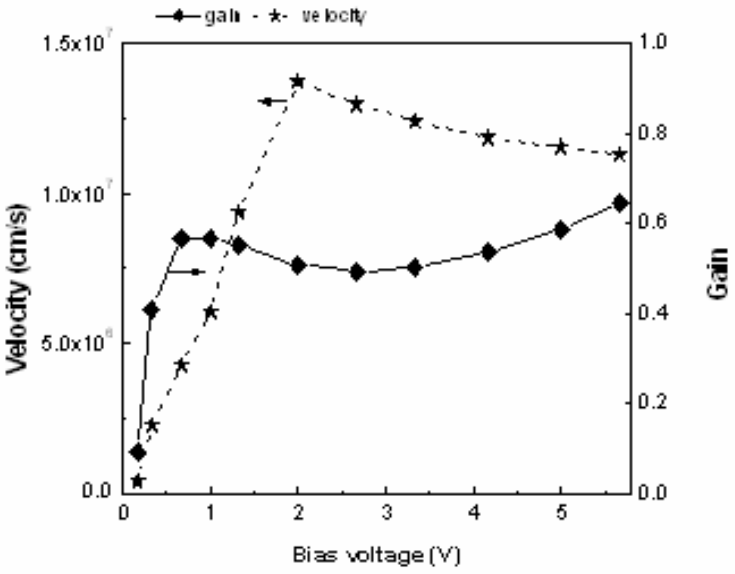

Figure 5.2: Calculated bias dependence of average electron velocity and gain

The gain characteristics determine the emitter field which is responsible for electron injection together with applied bias and the first well depletion. In the

program, one carrier is injected when another carrier reaches the connector. So the increase in the emitter field with bias depends on drift distance (g×L). Change of the emitter field and gain with bias are illustrated in Figure 5.3.

NDC is not observed in the emitter field characteristics. Rather, the rate of increase in the emitter field decreases under moderate bias (V>0.67V) where there is strong NDC in the gain. Local E-field distribution is given in Figure 5.4. The rate of increase at the emitter field with bias decreases by the effect of the NDC in the gain. Although, the average velocity decreases under high bias as seen in Figure 5.2, gain and the emitter field increase with almost equal rate as seen in Figure 5.3. This indicates an increase in the lifetime of electrons. The current injected from the emitter field, together with local capture probability, influence the charge densities in wells and barriers.

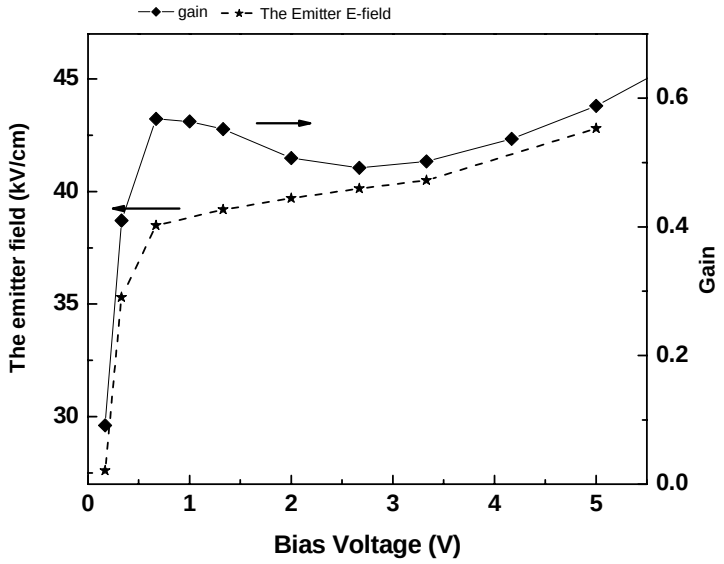

Figure 5.3: Calculated bias dependence of the emitter field and gain.

Local E-field distribution is illustrated in Figure 5.4. The difference between the electric fields in the barriers neighboring the wells is determined by the charge in each well. Under large photoexcitation rate, there is large charge density due to

low drift, so larger current density flows in barriers when it is compared with the dark current case. The injection current must be equal to the photocurrent in the steady state; thus, under small bias, most of the bias voltage drops on a small region near the emitter, and the E-field in the rest of device is weak, as previously suggested [10, 90]. When the bias is increased, the E-field extends through device.

The first well is depleted under large enough photoexcitation rates to increase the emitter field for supplying necessary current. Photoexcitation rate is independent of bias; however the emitter field depends on bias since drift distance changes with local E-field which determines velocity and capture [34, 35]. So the rate of increase of the emitter field with bias is not the same as in the bulk field. The bulk field is not only determined from the applied bias but it also depends on local effects, like capture.

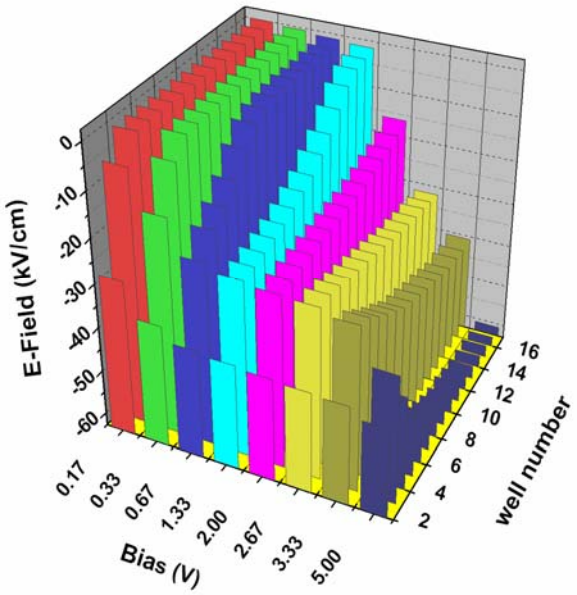

Figure 5.4: Local E-Field distribution

Beyond a bias of 2V, electron's velocity is constant with its saturated value and is uniform throughout the device under such a high and uniform electric field in

the bulk; therefore electron density in the barriers must be uniform and increase with bias due to an increase in the emitter field, as seen in Figure 5.7. Increase in the current density with bias due to emitter field also results in an increase in the charge density in wells by capturing electrons, as seen in Figure 5.8.

Accumulation starts to appear in the wells near the emitter as the applied bias increases enough to distribute large E-field in bulk which even exceeds the emitter field. The accumulation decreases the rate of increase at the emitter field; the rate of increase in current is low in bulk since electron velocity saturates. The non-uniform accumulation indicates non-uniform capture probability. The well accumulation occurs in a few wells near the emitter, and then it disappears.

The change of average barrier electron velocity throughout the device is determined by local E-fields, as seen in Figure 5.5. In barriers near the emitter, the order of the average barrier velocity does not change significantly (under 0.33-3.33 V) since the E-field itself does not change considerably (~35-45 kV/cm). The higher value of average velocity on the first barrier means that most of the electrons lie on Γ-valley with high energy. In bulk region, under 0.33V, the uniform and relatively very small velocity is a result of a uniform and very small E-field (~ 5 kV/cm) distribution, as seen in Figure 5.4. The average velocity saturates mainly in the third barrier under sufficiently large biases.

Under 1,33V, the velocity saturates near the emitter where E-field is large and, as the field decreases toward the collector, the average barrier velocity also adapts to this change. Under 2V or beyond, the large E-field is distributed uniformly, so the average velocity is uniform throughout the bulk region with the saturated value. There is a slight decrease in the average velocity under 3.33V, due to transition to the X valley where electrons see a barrier at heterojunction.

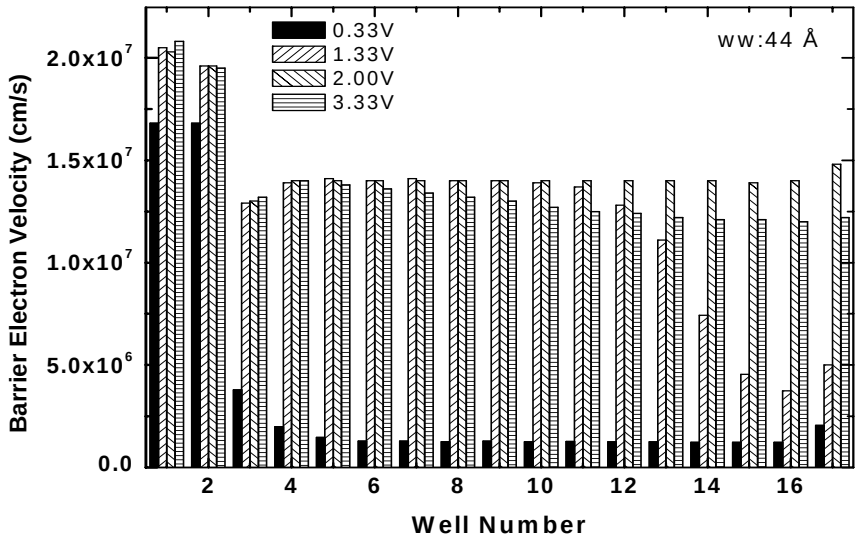

Figure 5.5: Barrier electron velocities in the QWIP structure with 44 Å thick wells.

It is thought that electrons move with saturated velocity in the bulk of the QWIP structure under sufficiently large bias [33, 34]. Electron transport in a QWIP is different from that in bulk because of reflection at interfaces and the velocity overshoot of newly excited electrons. At low electric fields, the velocity is much lower than that in bulk which is consistent with experimental observation [33, 34].

The barrier electron density is given in Figure 5.6. Under 0.33V bias, a uniform and small electric field results in very small electron velocity in the bulk region. The constant photoexcitation rate results in an increase in the barrier electron density due to low E-field. On the other hand, a small number of electrons in the first barriers move with large velocity since large portion of electric field is on emitter which is necessary for injection of electrons and the rest is distributed in the following few wells. The current density is given as

$$J = nqv, \tag{5.1}$$

where n is the number of electrons and v is the drift velocity. Although, the electric field strength can change throughout the structure, change in the drift velocity is compensated with charge density; therefore the current density is conserved on each barrier and throughout the device. Under 1.33V bias, the field distribution is non-uniform and it decreases dramatically on the final barriers where the drift velocity decreases due to low electric field and the number of electrons increases. Under higher bias voltage, both velocity and barrier densities are distributed uniformly in barriers throughout the structure. As bias voltage is increased further, it results in larger barrier densities due to higher injection.

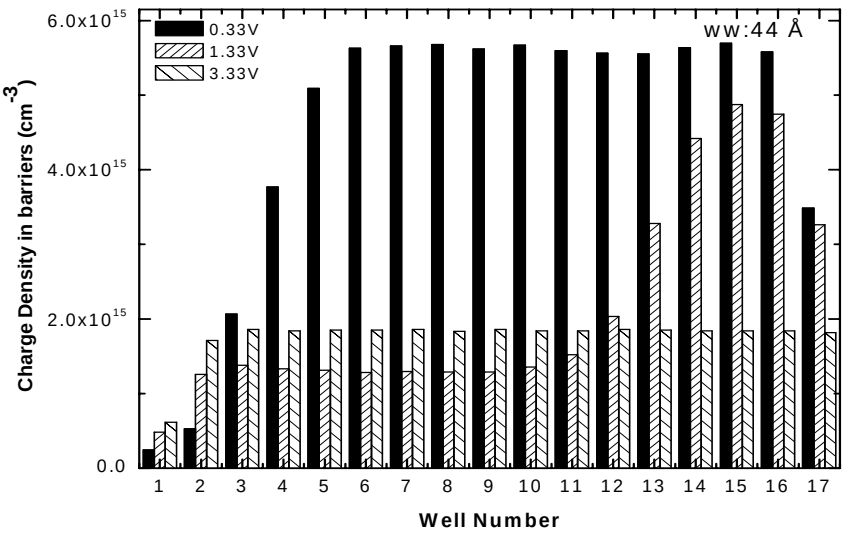

Figure 5.6: Barrier charge density in the QWIP structure with 44 Å thick wells.

Figure 5.7 shows charge densities in wells for the QWIP structures with 44 Å well width. There is strong depletion in the first well, as stated above. Depletion in the first well decreases with increasing applied bias since the emitter field increases and it determines the number of injected electrons. The amount of charge in the first well depends on the injected electron density and the local

capture probability. The local capture is discussed below. Carrier depletion or accumulation is reported by Pan and Fonstand, in their numerical work [90].

In bulk region, under small bias, the barrier charge density is high, but the electron velocity is relatively low. This result indicates that the capture probability is small in this range (0.17-0.67 V). Beyond 2 V biases where electric field becomes high and uniformly distributed throughout the bulk region of device, electrons drift with a uniform saturated velocity. In the bias range of (2.00-3.33 V), the well accumulation is also uniform and relatively high, contrasting their lower barrier electron density. These characteristics can be explained with high local capture probability. When the bias is increased further (5V), the well electron concentration decreases in spite of increase in barrier charge density. This shows a decrease in local capture probability under this bias

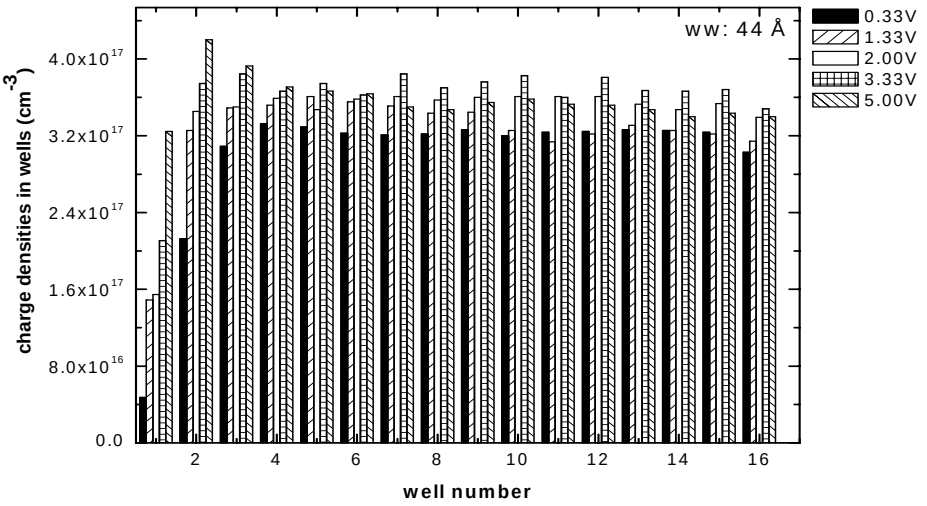

Figure 5.7: Well charge densities for QWIP with higher L QW discontinuity.

It is supposed that the capture probability decreases with E-field since the capturing via L-valley is not taken into account. Electrons in the Γ have large kinetic energy due to faster heating rate in the barrier and their high momentum in growth direction decreases the capture probability. In $Al_xGa_{1-x}As/GaAs$ with

~0.3 mole fraction, there is a close energy separation between Γ and L valley which increases the electron population in L-valley as well as a quantum well exist in L, as seen in Figure 5.1. The electron population in L-valley is given in Figure 5.8. Such a quantum well might affect the transport significantly since captured electrons cool in a well, then they can get scattered to continuum or main quantum well (Γ-QW).

Local capture probability (p_c) which is calculated by dividing the portion of the current captured by a well to the total current incident on the well is illustrated in Figure 5.8. An increase in p_c with increasing E-field is observed under intermediate E- fields (~10-20 kV/cm) where electron density in L-valley increases abruptly and the L-valley occupancy reaches ~ 40%. Thus, the sudden increase in the local capture probability in this region is interpreted as the impact of L-valley on capturing for $Al_{0.3}Ga_{0.7}As$/GaAs QWIPs. The capture probability decreases under higher E- fields where the electrons gain large energy in all valleys including the L valley. Hotter electrons in L need more phonon emissions to scatter to the L-QW. In the following sections the importance of the height of L-QW for capturing is discussed.

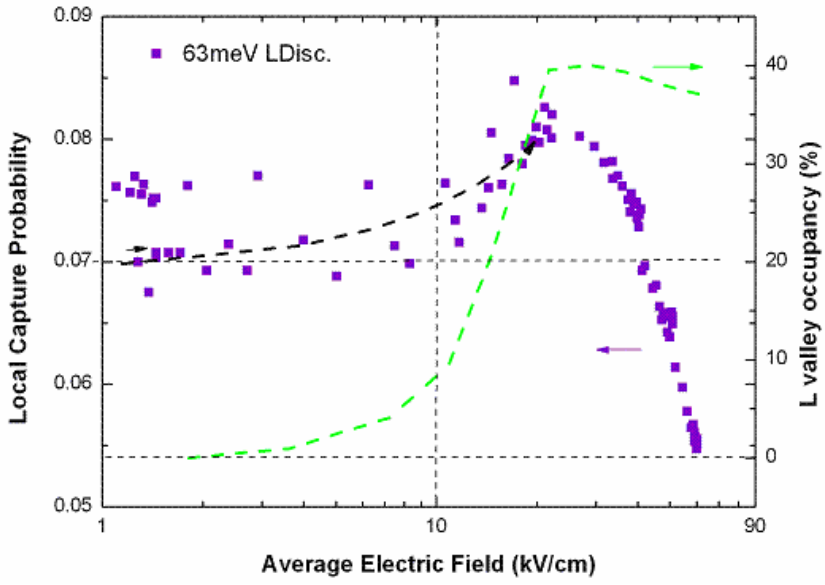

Figure 5.8: Calculated local capture probability for $Al_3Ga_{0.7}As$/GaAs QWIPs.

The spatial distribution of the captured electrons that are excited from various wells in the $Al_{0.3}Ga_{0.7}As$/GaAs QWIP under 1.33 V bias is given in Figure 5.9. It is commonly believed that the excited electrons experience the same capture probability in the following wells. Depending on the local E-field, electrons excited from a well are captured by the following wells with unequal probability. The first well following the well of excitation, captures the least number of electrons, while the third well captures the maximum number of electrons in the region under moderately high E-field. This is due to the heating of the newly excited electrons and their scattering to L valley resulting in an increase in their capture probability as they travel through a distance of approximately three periods from the well of excitation. Newly excited electrons become indistinguishable after travelling through this distance beyond which they exhibit capture characteristics similar to that usually assumed, under the given E-field strength. The distance mentioned above is reduced to two periods from the well of excitation, under 3.33 V bias. It should also be noted that the electrons excited from the wells near the collector (low E-field region) are most likely to be captured by the same well, and they can be even captured by the preceding wells due to the reflections from the hetero-interfaces.

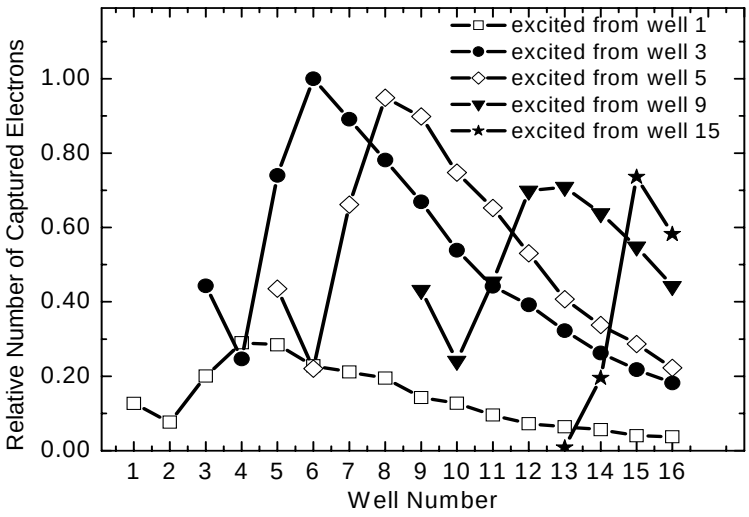

Figure 5.9: Spatial distribution of the captured electrons that are excited from various wells in the $Al_{0.3}Ga_{0.7}As/GaAs$ QWIP under 1.33 V.

An increase in capturing results in a decrease of electron drift length under intermediate E-fields (~10-40 kV/cm); thus the gain decreases in this range. The NDC in $Al_{0.3}Ga_{0.7}As/GaAs$ QWIPs is discussed at the beginning of this section. The bias voltage range where the NDC is observed, in Figure 5.2 is the same region where capturing from L-valley is effective. So, the NDC in $Al_{0.3}Ga_{0.7}As/GaAs$ QWIPs can be explained as its structure is suitable for capturing from L valley and this decreases the lifetime electrons. The bias voltage dependence of the lifetime of electrons is given in Figure 5.10. The lifetime of electrons increases under large biases due to a decrease in the capture probability because of heating in the satellite valleys. The gain also increases under large biases, as shown in Figure 5.2 and this can be related to an increase in the lifetime of electrons due to the decrease in capturing.

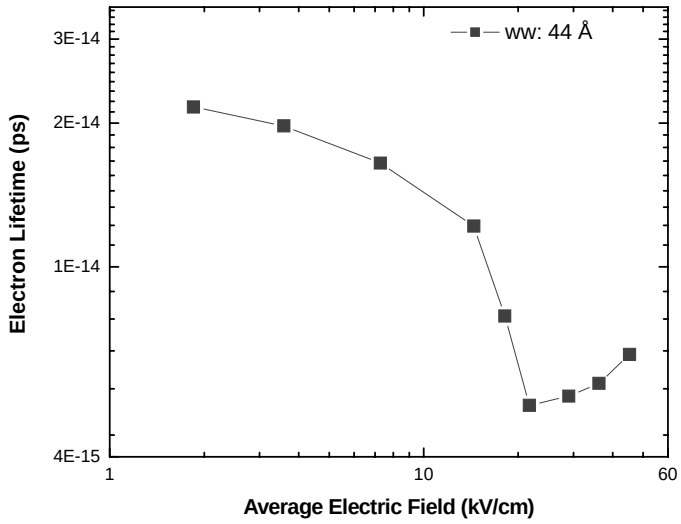

Figure 5.10: Average electron lifetime vs. the average electric field in $Al_{0.3}Ga_{0.7}As/GaAs$ QWIPs**.**

5.2 Local Capture Probability in QWIP

5.2.1 Effect of L Quantum Well Discontinuities on Capturing

The height of quantum well in L-valley is artificially increased from 63 to 95 meV. The energy levels and wave functions are calculated according to new L-QW height. Necessary scattering rates of L valley are recalculated using the new wave functions.

Figure 5.11 shows scattering rates in L for both 63 and 95 meV L-valley discontinuities. Since there are four alternative final sites for the electrons scattering from Γ to L subband and three alternative final sites when they do intravalley scattering in the L subband, the scattering rates for transitions to L or inside L are significantly high when electrons have enough energy. Their relatively large effective mass in L also increases the scattering rates for electrons into L.

Both intra-valley and inter-valley scattering rates are calculated by using deformation-potential interaction. Polar optical scattering (POP) which is effective in compound semiconductors is used for intra-valley scattering calculations. The 2D POP scattering rates includes the effect of dielectric screening [99].

The intervalley scattering rate for transition between Γ and L subbands with phonon emission is more probable if electrons have high energy to allow it, as seen in Figure 5.11.a. Electrons are quite likely to lose energy by equivalent-intervalley scattering with phonon emission in L subband. The intervalley scattering from L to Γ-subband is significantly high which enhances capturing. The transition of electrons between continuum and bound states is modelled as 3D↔2D POP scattering [96]. The rates of capturing of electrons by L-QW are given in Figure 5.11.b. These rates are large enough to be taken into account.

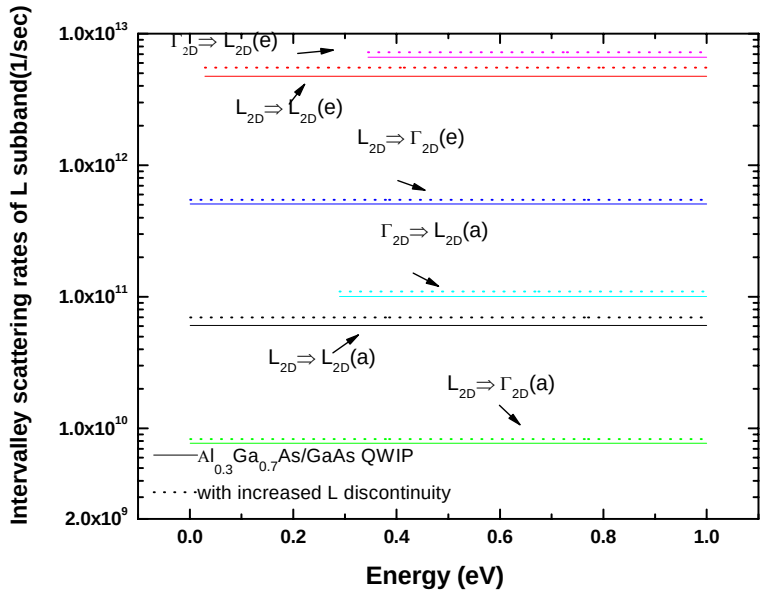

(a)

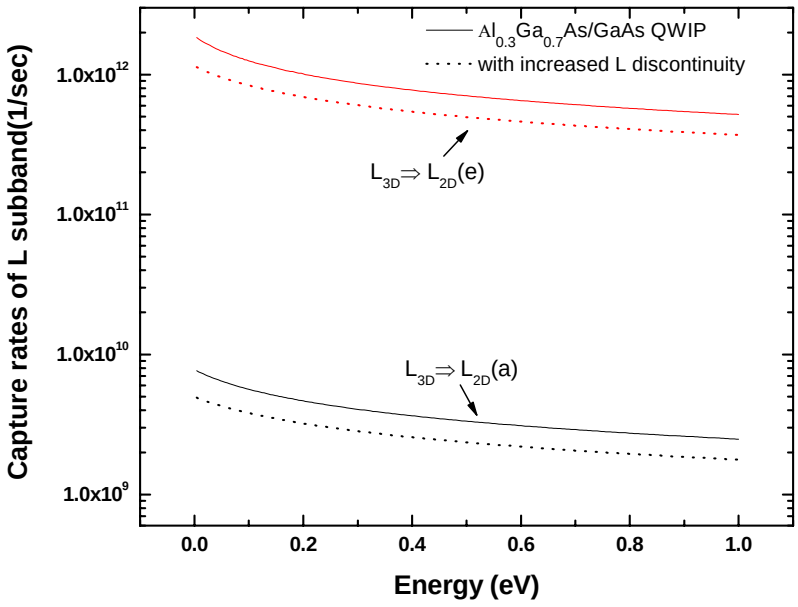

(b)

Figure 5.11: L related scattering rates: (a) inside L subband (b) into L subband.

Figures 5.12 and 5.13 show the percentages of effective scattering rates in continuum and the subband of L for both 95 and 63 meV L discontinuity cases, respectively. The capture mechanism via L-QW is as follows; first, continuum L electrons are captured into the L subband by 3D↔2D POP emission. After this, during the equivalent intervalley scattering, they lose their energy with phonon emissions in the well. The rate of capturing by L-subband decreases ($L_{2D}\leftrightarrow\Gamma_{2D}$) from 64.2 % to 39.2 % because of increasing energy levels between these states, as given in Figure 5.12.b and 5.13.b, but the cooling rates increase in the L subband for the structure with larger height in the L-QW which is caused by the increase in the equivalent- intervalley and intravalley scatterings.

The main path of the capture process is a transition from the L to the Γ subbands via the intervalley phonon scattering. Phonon emission with equivalent-intervalley scattering is more probable in the structure with higher L-QW height. Cooling rates for both in L-continuum and inside L-QW are high for these two structures but they are more significant in large L discontinuity case, especially inside L subband, as given in Figures 5.3 and 5.4. The scattering rate between $L_{3D}\leftrightarrow L_{3D}$ does not change in L continuum by increasing the L-QW height, but the change of the rate in $L_{3D}\leftrightarrow L_{2D}$ establishes a new balance between the scattering rates in L-continuum towards increasing phonon emission. This increases the capture by the Γ-subband regardless of the capture mechanism. It might be due to the nonequivalent intervalley scattering from L to Γ subbands or electrons originating from Γ-continuum to Γ-subband via polar optical phonon emission.

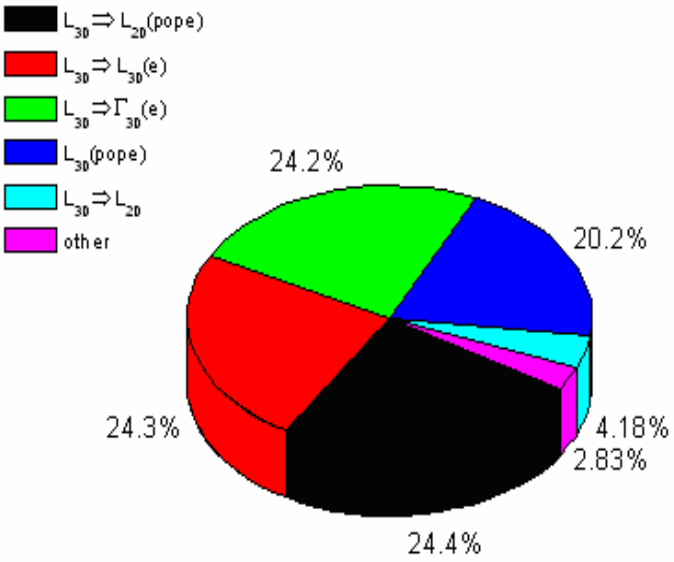

(a)

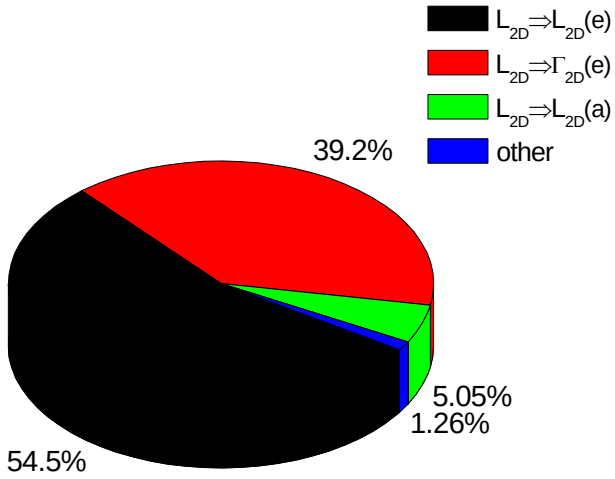

(b)

Figure 5.12: Portions of the effective scattering rates a) in L continuum valley and b) inside L subband for 95meV L-QW discontinuity.

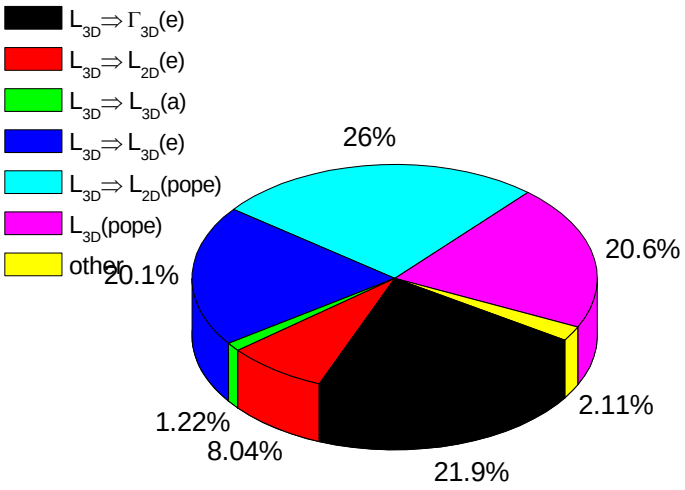

(a)

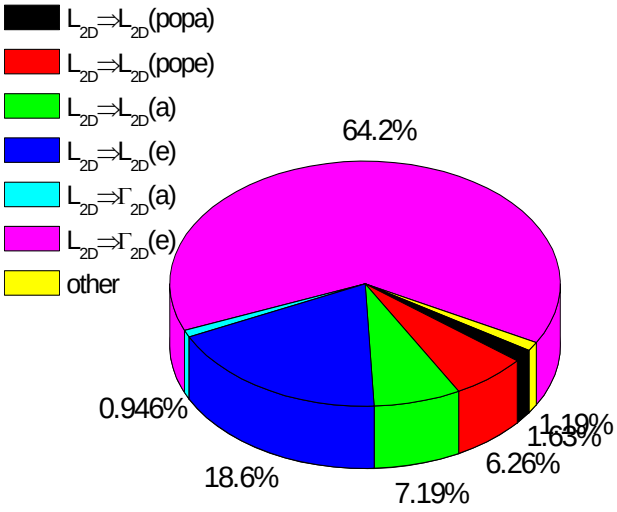

(b)

Figure 5.13: Percentages of the effective scattering rates a) in L continuum valley b) inside L subband for 63 meV L-QW discontinuity.

Figure 5.14 illustrates local capture probabilities, for both 63 and 95 meV L-QW discontinuities. The concept of capture probability which was first used in QWIP by Liu [77] is defined as the fraction of photoelectrons recombined in a particular quantum well and total photocurrent passing through that well. The Ensemble Monte Carlo program enables us to count every captured electron; so, the local capture probability is calculated by taking the ratio of number of captured electrons to total number of electrons passing through each well under various electric fields for a certain time interval. An electron which falls into the Γ-subband and loses its kinetic energy is defined as a captured electron.

Higher cooling rates in the L-subband by phonon emission during equivalent-intervalley scattering results in a significant increase in local capture probability for QWIPs with larger L discontinuity; because hot electrons scattered to Γ-subband can easily be re-scattered to Γ-continuum or L-subband due to their high energies. Therefore, cooling in L-subband contributes to the capture of electrons by decreasing the average energy of the newly captured electrons. In AlGaAs/GaAs QWIP structure with the aluminum mole fraction of 0.3, the L valley occupancy is significantly large (~40%) under moderate and large bias, as given in Figure 5.8. This increases the effect of capturing via L in such structures with satellite valleys close to Γ. In a typical $Al_{0.3}Ga_{0.7}As$/ GaAs QWIP structure, capture probability increases under moderate electric fields due to intervalley transitions between Γ and L where electrons find suitable paths for being captured.

The most frequent scattering rate in L subband is equivalent-intervalley scattering with emission of phonon which cools the electrons before their scattering to Γ where they are easily captured due to their low energies. The local capture probabilities are compared for these structures with L-QW heights of 63 and 95 meV in Figure 5.14. The increase in p_c with increasing E-fields is seen under the same range of E-fields. Having relatively high local capture

probabilities (×2) with increasing height of L-QW, in this region, indicates that L-QW behaves like a trap for capturing from L by cooling in the subband.

There is also an increase in the local probability in the range of ~0-10 kV/cm where electron population in Γ dominates; however the scattering rates for Γ. continuum do not change. So, this increase can be explained with other parameters; e.g. the emitter field, the local E-field and velocity distribution. It can be attributed also to capturing low-energetic electrons in L-valley as discussed above.

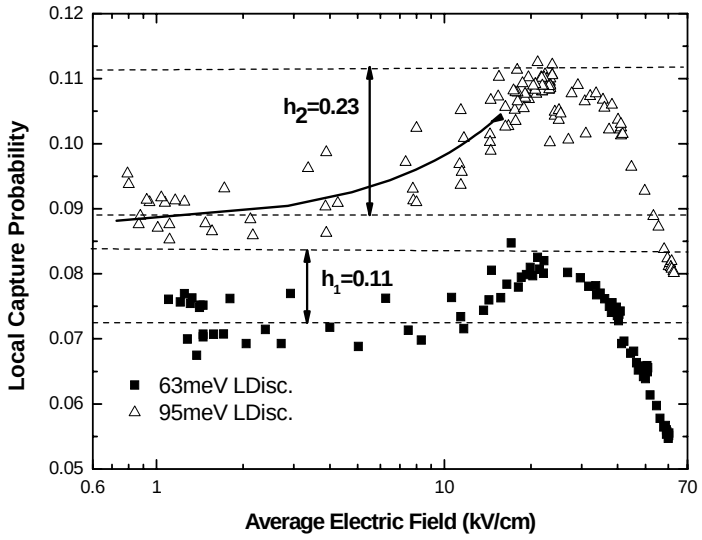

Figure 5.14: Local capture probability for QWIP structures with different L-QW discontinuity.

5.2.2 Effect of Well Width on Capturing

The effects of shortening the quantum well width are different on different scattering rates. The capture and escape rates are shown in Figure 5.15. We can conclude that the new scattering rates change in a way that capture events decrease with shortening well width from 44 to 36 Å.

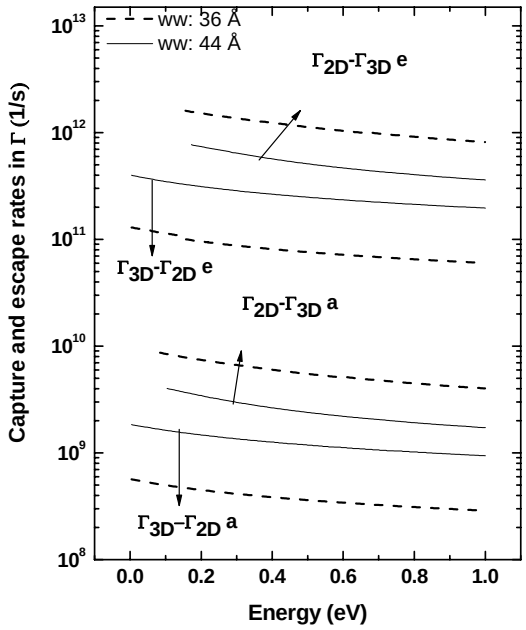

(a)

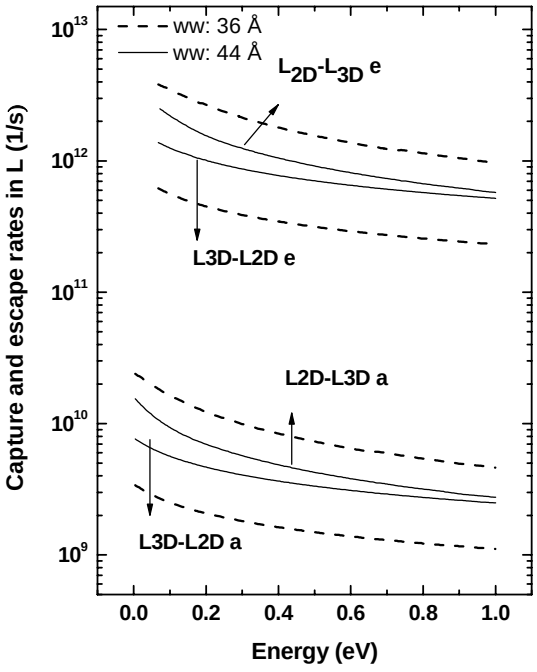

(b)

Figure 5.15: Capture and escape scattering rates a) in Γ-valley b) in L-valley

The comparison of the local capture probabilities for the two QWIP structures with different well widths is given in Figure 5.16. The local capture probability is almost halved for the structure with relatively longer well widths. Shortening well width decreases the possibility of making any scattering in the well region including capture related scattering. The increase in p_c with increasing E-field under intermediate E-fields is less significant in the shorter well width device. Under large E-fields, p_c decreases with increasing field due to heating of the electrons in the satellite valleys.

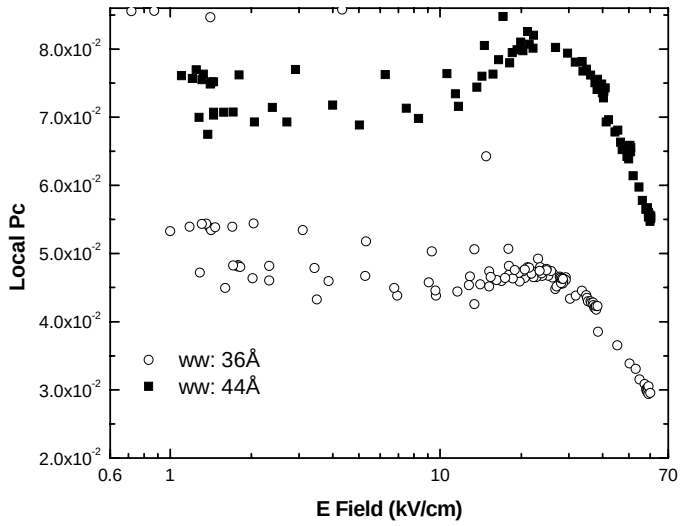

Figure 5.16: Local capture probability of QWIP structures with different well widths.

5.2.3 Effect of Various Parameters on Capturing

Figure 5.17 shows local capture probabilities in various QWIP structures [35]. In $Al_{0.3}$ $Ga_{0.7}As$/GaAs QWIP, the local capture characteristics are discussed above. It is observed that depending on the material parameters, capture probability may increase with increasing electric field which is in conflict with the general belief that local capture probability monotonically decreases with increasing electric field. The effect of capturing via L valley is more effective in the QWIP

structure where electron effective mass is halved artificially, since the velocity has saturated under lower electric field if electrons have small effective mass. This results in higher L valley population so local capture probability reach the maximum value under moderate bias.

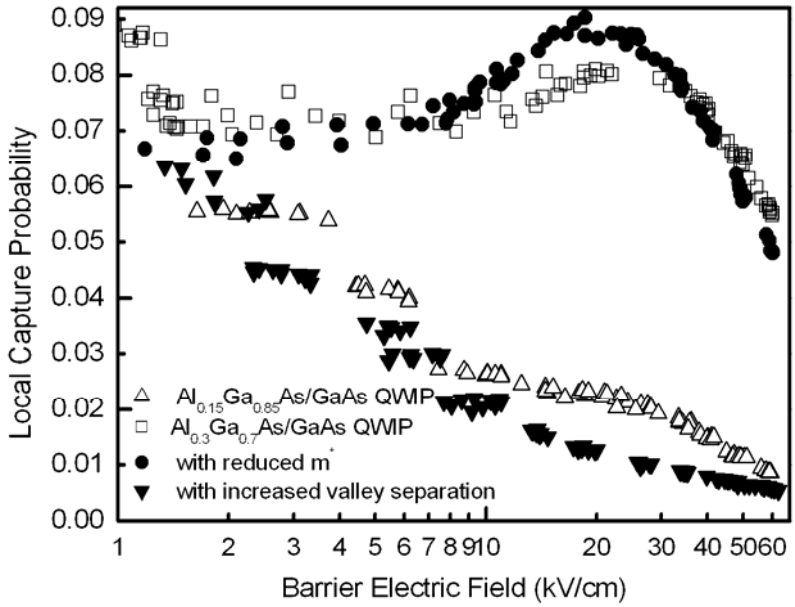

Figure 5.17: Calculated local capture probabilities vs. the electric field in various QWIP structures [35].

In $Al_{0.15}Ga_{0.85}As/GaAs$ QWIP structure, local capture probability is much smaller and decrease with increasing electric field when it is compared with the AlGaAs/GaAs QWIP structure with 0.3 Al mole fraction [35]. This small capture probability can be explained with larger Γ-L spacing and the shallower L-QW height in the structure. The capture probability is in the same order with $Al_{0.15}Ga_{0.85}As/GaAs$ QWIP structure in the QWIP structure with increased valley separation.

Increasing Γ-L spacing affects scattering rate significantly; electrons in the L subband might choose the scattering path L-subband to Γ-continuum or L-continuum rather than the scattering path from L to Γ subband [35]. So, selecting

the material determines the device performance. For example, using InP in the IR detector fabrication has a good advantage due to low capture probability which indicates high gain performance under intermediate biases.

5. 3 Well Charge Densities

Figures 5.18 and 5.19 show the charge densities in wells for the QWIP structure with 36 Å well widths and for larger L-QW discontinuity, respectively. As discussed below, depletion in the first well decreases with increasing applied bias since the emitter field increases. Bias dependence of the emitter field of these structures is shown in Figure 5.20. Well charge increases with bias under moderate bias where the capture probability takes maximum value and the increase in the total current enhances the well charge density. Charge densities in the wells are relatively higher in the structure with higher L-QW due to large local capture probability. As a result of larger emitter field nature, the well accumulation near emitter is also larger for the QWIP structure with 36 Å thick wells.

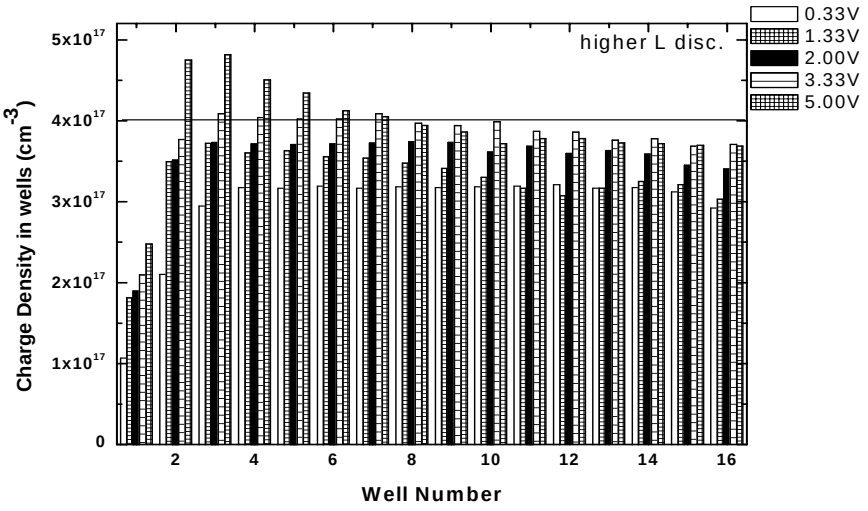

Figure 5.18: Well charge densities for QWIP with higher L-QW discontinuity.

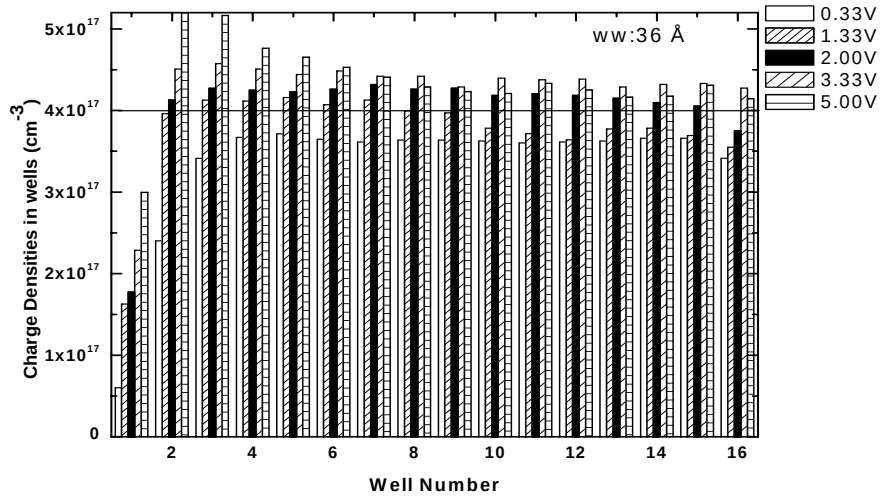

Figure 5.19: Well charge densities for QWIP with 36 Å thick wells.

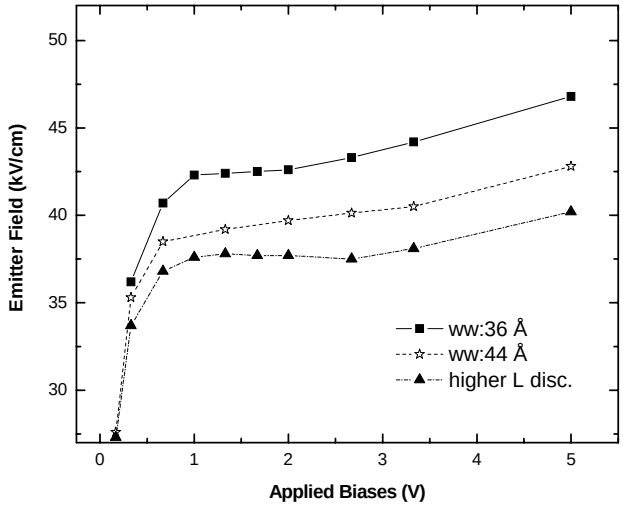

Figure 5.20: Emitter field vs. applied bias

5. 4 Electric Field Profile in QWIPs

The charge in each well determines the difference between the electric fields in the barriers neighboring the wells. Increased electron concentration in the well is reflected in Figure 5.21 in which electric field profiles of QWIP structures with different L-QW height are compared. Both electric fields at bulk and the emitter decrease since drift length decreases due to higher capture rate in the structure with high L-QW height. In a typical QWIP operation, most of the electric field is distributed near the emitter region and the electric field at bulk region is very small under low bias. The current density created by small numbers of electrons with large drift velocity near the emitter region and a large numbers of electrons with low drift velocity at bulk region.

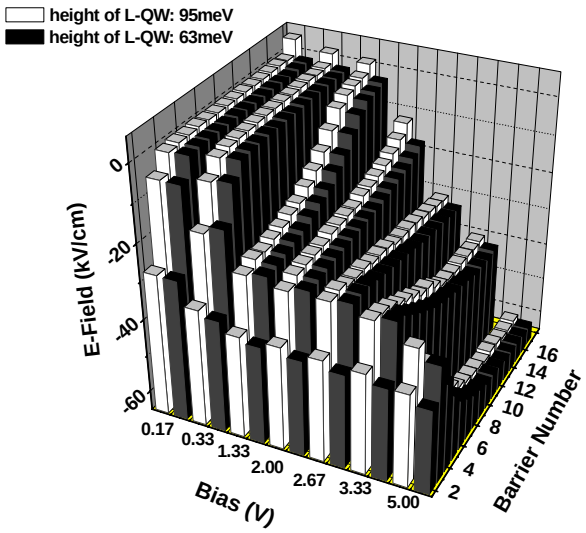

Figure 5.21: Electric field distributions for QWIP structure with different L-QW height.

Figure 5.22 compares the electric field profiles of QWIP structures with different well widths, 36 and 44 Å. Shortening the well width decreases the local capture probability so gain or drift distance in the device increases, so does the emitter field. Larger current density increases the accumulation region in the

second and the following wells under large bias. At the wells near the contacts, the electric field increases due to lower local capture probability.

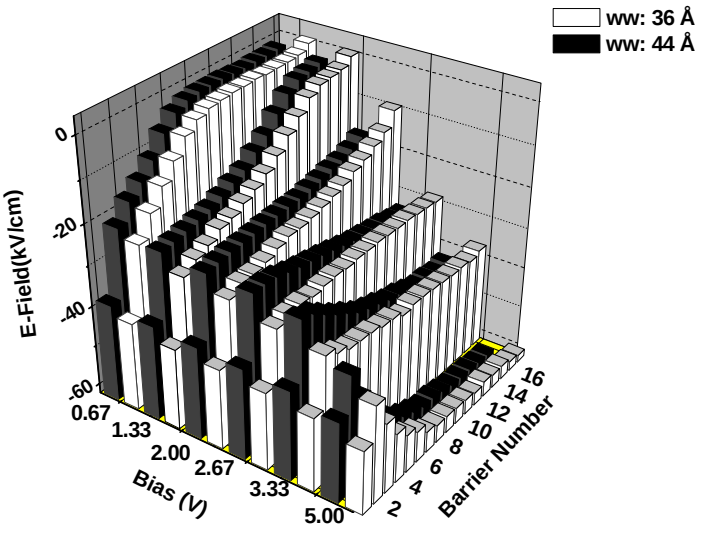

Figure 5.22: Electric-field distributions for QWIP structure with different well widths

5.5 Barrier Charge Densities and Velocities

Figures 5.23 and 5.24 illustrate barrier charge densities and barrier electron velocities in the QWIP structures with 36 Å thick wells, respectively. Although, the electric field strength can change throughout the structure, change in the drift velocity is compensated with charge density; therefore the current density is conserved on each barrier and throughout the device. For example, under very low bias, electrons have very high velocities on first wells since large portion of electric field is on emitter which is necessary for injection of electrons, and on the barrier electron density is relatively low. On the other hand, the average velocity sharply decreases in the bulk region due to low electric field strength but the electron density increases to conserve the current passing through the

structure. Under 1.33 V bias, the field distribution is non-uniform and it decreases dramatically on the final barriers where the drift velocity decreases due to low electric field and the number of electrons increases. Under higher bias both velocity and barrier densities are distributed uniformly in barriers throughout the structure.

Barrier charge densities are relatively high in the QWIP structure with 36 Å thick wells due to high current density. As the applied bias is switched to 5 V, the increase in the current is reflected by increasing the barrier density since the electric field is high enough to saturate the electron velocity beyond 2 V bias as seen in Figure 5.23. Larger emitter field causes higher average velocities on the first barriers and a sharp decrease of the velocity in the second barrier can be the indication of significant amount of electrons that are saturated. However the QWIP structure with 44 Å has also large average velocity in the second barrier. Under moderate and large bias, the average velocity is a bit lower in the bulk region of the device where local capture probability is small and electrons are travelling mostly on the satellite valleys which decrease average velocity in the structure with shorter well thickness.

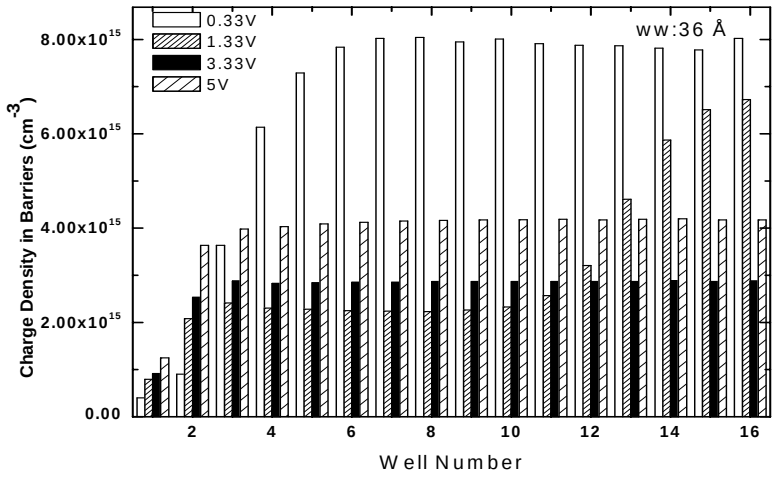

Figure 5.23: Barrier charge densities in the QWIP structure with 36 Å thick wells.

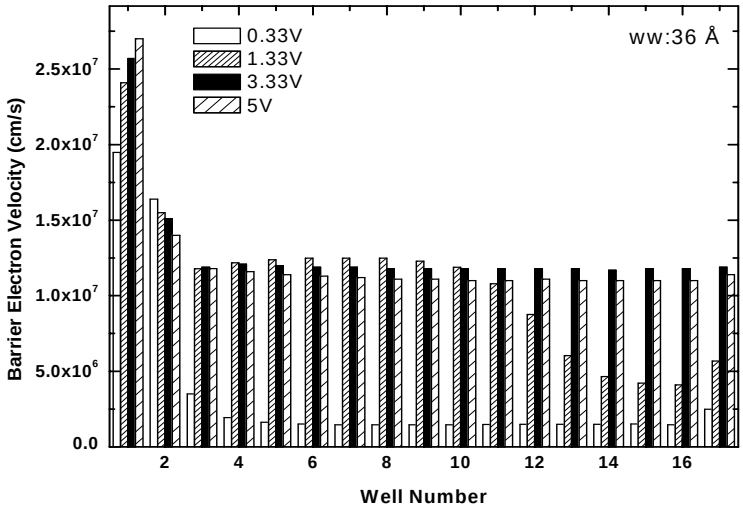

Figure 5.24: Barrier electron velocities in the QWIP structure with 36 Å thick wells

5. 6 Gain, Electron Velocity and Excited Electron Lifetime

The gain of QWIPs is usually extracted from noise measurements [108, 109, 113]. The gain can be expressed as L_d/L where L_d is the drift distance of the excited electrons, and L is the total device length. The gain of $Al_xGa_{1-x}As/GaAs$ QWIP with x~0.3 exhibits negative differential change beyond ~2 V for a 50-well device [108, 109]. The negative differential change in the gain was attributed to ground state sequential tunnelling by Levine *et al.* [108] and to the degradation of transport properties through intervalley transfer in the barriers by Schneider *et al.* [109]

Figure 5.25 shows the calculated drift distance versus the average E-field in the device for two simulated QWIP structures with different L-QW heights. Drift distance is extracted from the device gain obtained by dividing the number of electrons injected into the device by the total number of the excited electrons

that escape from QWs, which is equal to the total number of captured electrons at steady-state [114].

The drift distance depends on electric field profile and it is determined by the mobility and the capture probability which is an impact parameter that determines the lifetime of excited electron for structures whose capture rates are significantly high. A negative differential change (NDC) is observed in the drift distance versus E-field characteristics of $Al_{0.3}Ga_{0.7}As$/GaAs QWIP and the same structure with artificially increased energy barrier for L-QW [34, 35, 115], as shown in Figure 5.25. The shorter drift distance might be a result of trapping of electrons in the L-QW in addition to the increase in the capture rate as seen in Figure 5.5. The divergence of NDC is slightly smaller for the structure with higher L-QW height due to their slightly lower average velocities and almost equal lifetimes. The comparison of averaged velocities of barrier electrons and lifetimes of electrons at different electric fields are given in Figures 5.26 and 5.27 for both structures, respectively. The lower average electron velocity in the structure with higher height of L-QW is a result of the decrease in the electric field under small bias. In addition to lower E-field distribution, as the applied bias increases the electron population in the L valley increases, so the energy loss is significant on this valley continuum and in its subband. This effect is much greater for the structure with higher height of L-QW. Experimental results indicate that $Al_xGa_{1-x}As$/GaAs structure with lower Al mole fraction has higher drift distance [110, 115]. By lowering the Al mol fraction, L-QW height becomes shallow so capture probability decreases in that structure in addition to having hotter electrons which result in high gain characteristics.

The lifetime of excited electrons is longer under small electric fields due to their lower kinetic energy and then it decreases with increasing electric field in the structure with higher L-QW. The lifetimes are very short at moderate electric fields where the capture probability reaches the maximum value. Then, as the bias is increased, lower lifetime is seen in the structure with higher L-QW due to larger capture probability. Actually, the lifetime in the figure does not really

reflect the decrease in capture probability as seen in drift distance comparison; the reason might be the time lost in the L-QW which causes longer electron lifetime.

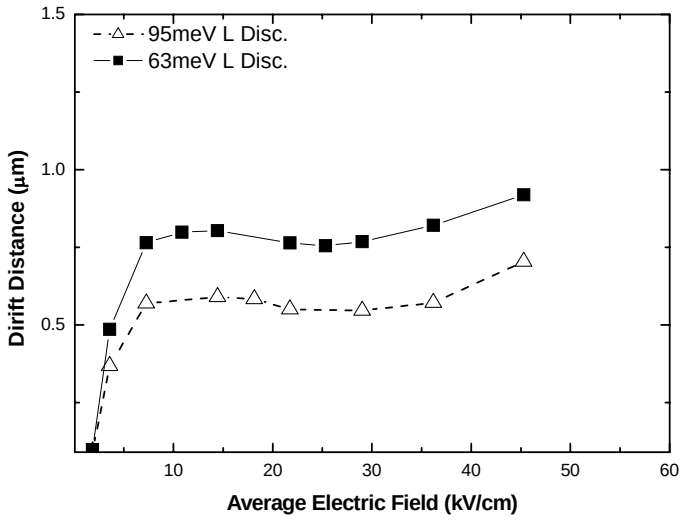

Figure 5.25: Drift distance vs. average velocity in QWIP structures with different L-QW height

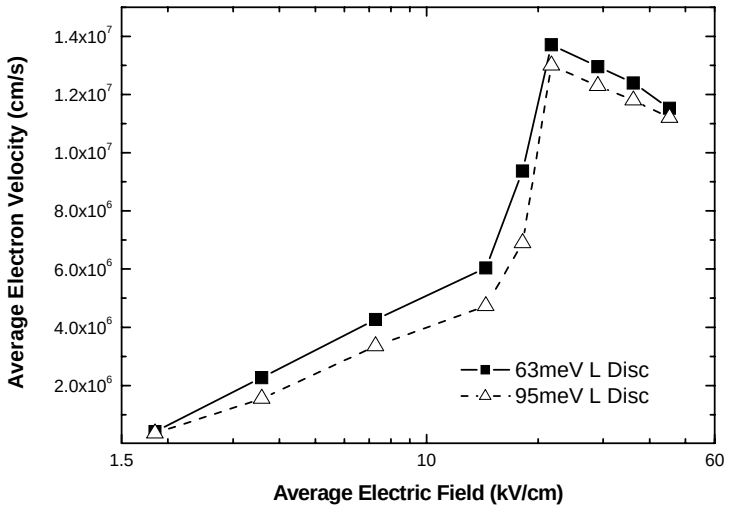

Figure 5.26: Average electron velocity vs. average electric field in QWIP structures with different L-QW height.

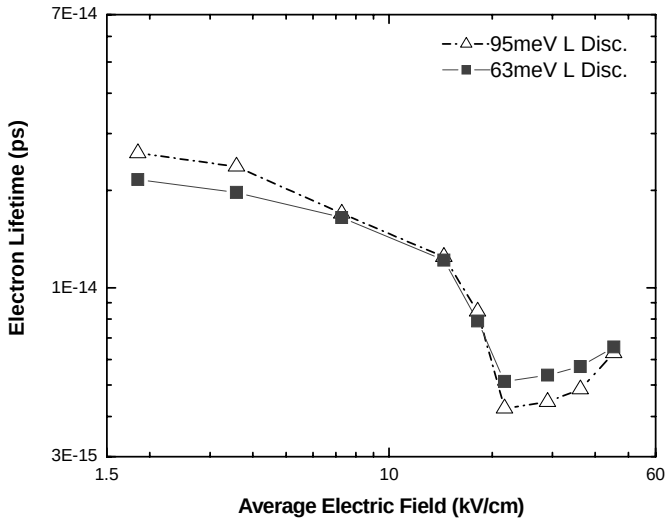

Figure5.27: Average electron lifetime vs. average electric field in QWIP structures with different L-QW height.

The well length is also an important variable which affects the QWIP figures of merit for a standard $Al_{0.3}Ga_{0.7}As/GaAs$ structure. Figure 5.28 shows the calculated drift distance versus the average electric field in the device. As the well length is shortened the drift distance increases. The average electron velocity is slightly lower in the shorter well QWIPs, as shown in Figure 5.29. This slight decrease in average velocity under moderate and large bias is a result of higher rate of electron occupancy in satellite valley due to lower capture probability. On the other hand, longer lifetime of excited electrons as seen in Figure 5.30 causes the longer drift distance for the structure with short well length. The longer lifetime can be explained by the large decrease in local capture probability; it is almost halved for the structure with lower well width. There is a slight negative differential change for this structure under the same range of electric fields where L valley occupancy increases significantly and excited electron lifetimes decrease and take minimum value in this region for both structures.

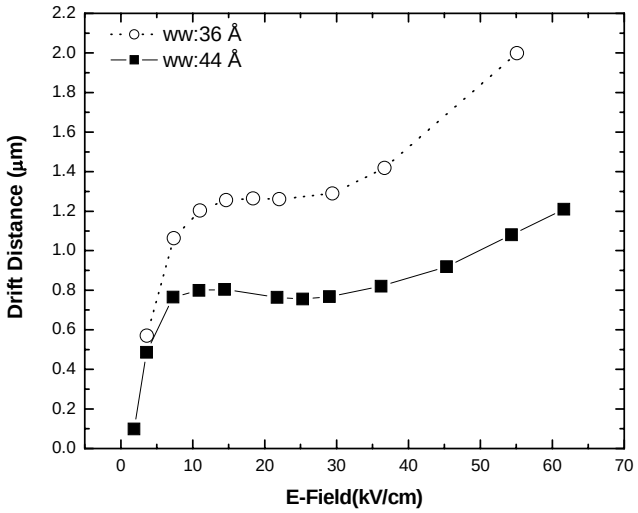

Figure 5.28: Calculated local capture probability versus the electric field in the barrier preceding the capturing quantum well in $Al_{0.3}Ga_{0.7}As/GaAs$ QWIP structures with various well widths.

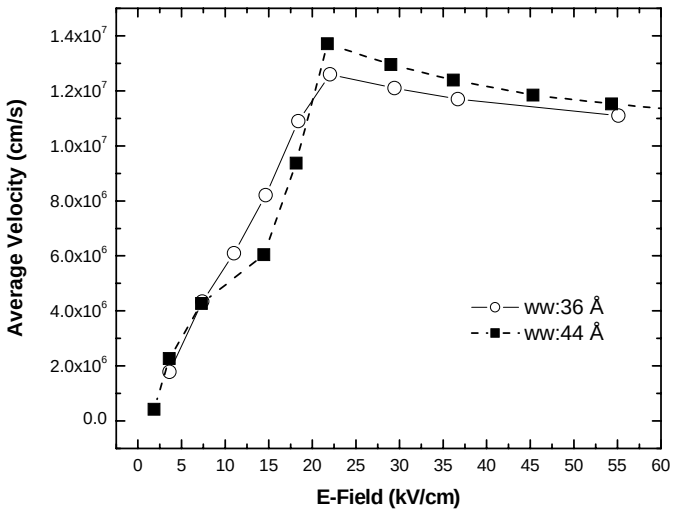

Figure 5.29: Average electron velocity versus average electric field in $Al_{0.3}Ga_{0.7}As/GaAs$ QWIP structures with various well widths.

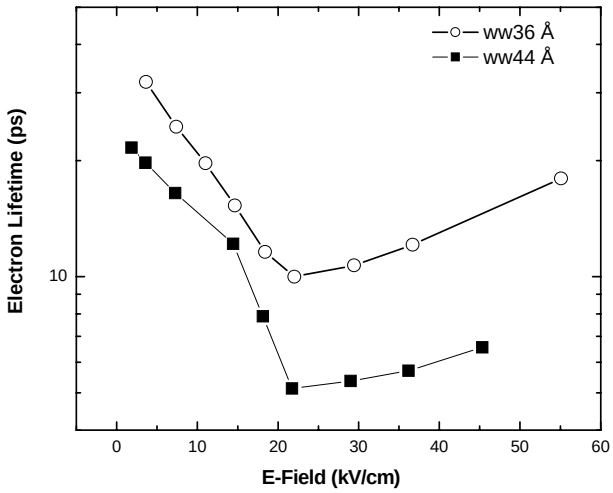

Figure 5.30: Average electron lifetime versus average electric field in $Al_{0.3}Ga_{0.7}As/GaAs$ QWIP structures with various well widths.

CHAPTER 6

CONCLUSION

We have performed detailed EMC simulations of QWIPs. The result of this work give a quantitative explanation of the different gain-bias characteristics observed on QWIPs based on various material systems. In order to provide a better understanding of the QWIP operations and characteristics, local changes are considered under various bias; E-fields in each barrier, average barrier velocity, well and barrier charge density, capture probability in each well, electron population and energy in each valley throughout the device.

We have mainly worked on electron transport and capture in $Al_{0.3}Ga_{0.7}As$/GaAs QWIPs. It is found that well accumulation occurs non-uniformly, being highest near the emitter under large bias. The barrier electron velocity in this QWIP is slightly larger than the electron saturation velocity in $Al_{0.3}Ga_{0.7}As$ due to overshoot in velocity of electrons which are excited from the preceding wells, under large barrier E-field. The velocity is much lower than that in bulk, under low electric fields due to reflections at interfaces. Non-uniform local p_c is observed which takes maximum value after overshooting if the electrons are traced for each source (the emitter or a well) to collector. We have observed that there is non-uniform change in average local p_c with E-field since the L valley plays a significant role in electron capture into QWs at $Al_{0.3}Ga_{0.7}As$/GaAs QWIPs. A NDC is observed in the gain characteristics of these QWIPs which

shows satisfactory agreement with the available experimental values. It is generally supposed that intervalley transfer affects the gain through the decrease in the electron drift velocity. Our calculations shows that the intervalley transport on the gain is two fold; the decrease in the electron velocity, and the decrease in exited electron lifetime since the p_c increases with the creation of an effective capture path in L-QW.

$Al_xGa_{1-x}As/GaAs$ QWIPs with barrier mole fraction lowered from 0.3 to 0.15 have been simulated to investigate the effect of changed parameters [35]. In the second configuration Γ-L separation increases and L-QW becomes shallower. These two fold factors in L-valley result in significant increase in the gain. The improvement in gain with decreasing mole fraction is in agreement with the experimental results. In order to make clear the effects of these parameters, namely; Γ-L separation, effective mass and height of L-QW, we have simulated $Al_{0.3}Ga_{0.7}As/GaAs$ QWIPs by changing just one parameter in each simulation.

The effective mass have been halved in Γ, L and X valley in another set of simulation of $Al_{0.3}Ga_{0.7}As/GaAs$ QWIPs [35], so the electron velocity saturates more easily in satellite valleys. Stronger NDC is observed which started at earlier bias due to lower lifetime of electrons. The local capture probability increases with higher rate at the E-fields where L electron population increases as well.

We have investigated the effect of the height of L-QW on QWIPs operation by simulating $Al_{0.3}Ga_{0.7}As/GaAs$ QWIPs with two different heights of L-QW. The local p_c significantly increases (×2) with small amount of increase in the height from 63 to 95 meV. The reason for this increase is cooling of electrons in the well rather than the rate of scattering path of $L_{2D} \leftrightarrow \Gamma_{2D}$ which actually decreases in the new configuration. They possess relatively low gain with stronger NDC. Accumulation in wells increases with increasing capture probability even in the case of a decrease in total current.

We have also simulated $Al_{0.3}Ga_{0.7}As/GaAs$ QWIPs by varying the well length from 44 Å to 36 Å. In the new configuration, the rate of decrease in the electron lifetime is lower due to a decrease in local p_c which is almost halved under moderate bias (i.e., probability of any scattering decreases with decreasing in the well lengths). Well accumulation increases due to higher current. The gain of this configuration is higher and NDC change in the gain weakens.

In summary, the selection of materials for QWIPs fabrication is critically important in terms of not only the central valley but also the configurations in the satellite valleys which can behave like a trap. Moreover, choosing materials which has higher energy spacing between the central and satellite valleys has a big advantage due to good transport properties in Γ valley with low capture probability for hotter electrons.

Although the results of our simulator are in good agreement with observations on the relative magnitude and the bias dependence of gain in QWIPs, including other scattering mechanisms will allow the simulator to approach realistic device operation more closely.

This program can be developed to a more compact form to obtain the characteristics of any QWIP structure by providing the input parameters such as well and barrier material, doping density, number of wells, well and barrier lengths. It can also be converted to simulate type II QWIPs and QDIPs.

REFERENCES

[1] A. Rogalski, *Infrared Photon Detectors*, SPIE press, 1995.

[2] H. C. Liu, *Intersubband Transitions in Quantum Wells: Physics and Device Applications I*, Semiconductors and Semimetals, **62**, Academic Press, 2000.

[3] M. A. Fauci, R. Breiter, W. Cabanski, W. Fick, R. Koch, J. Ziegler, and S. D. Gunapala, *Infrared Physics & Technology*, **42**, 337, 2001.

[4] W. A. Goddard, D. W. Brenner, S. E. Lyshevski, and G. J. Iafrate, *Handbook of Nanoscience Engineering and Technology*, CRC Press LLC, 2003.

[5] A. Goldberg, K. K. Choi, *Proceedings of SPIE*, **5406**, 624, 2004.

[6] L. Esaki and H. Sakaki, *IBM Tech. Discl. Bull*., **20**, 2456 (1977)

[7] M. J. Kane, S. Millidge, M. T. Emeny, D. Lee, D. R. P. Guy, C. R. Whitehpuse, *Intersubband Transitions in Quantum Wells*, eds. E. Rosencher, B. Vinter and B. Levine (Plenum, New York), pp. 31-42, 1992.

[8] P. Man and D. S. Pan, *Appl. Phys. Lett*., **66**, 192, 1995.

[9] C. H. Chu, C. I. Hung, Y. H. Wang, M. P. Huong, *IEEE Photon. Technol. Lett*., **9**, 1262, 1987.

[10] M. Ershov, V. Ryzhii and C. Hamaguchi, *Appl. Phys. Lett.,* **67**, 3147, 1995.

[11] M. Ershov, C. Hamaguchi and V. Ryzhii, *Jpn. J. Appl. Phys*., **35**, 1395, 1996.

[12] M. Ershov, H. C. Liu, L. Li, M. Buchanan, Z. R. Wasilewski and V. Ryzhii, *Appl. Phys. Lett.,* **70**, 414, 1997.

[13] M. Ershov, H. C. Liu, L. Li, M. Buchanan, Z. R. Wasilewski and V. Ryzhii, *Appl. Phys. Lett*., **70**, 1828, 1997.

[14] L. Thibaudeau, P. Bois and J. Y. Duboz*, J. Appl. Phys*., **79,** 446, 1996.

[15] V. Ryzhii, *J. Appl. Phys.,* **81**, 6442, 1997.

[16] V. Ryzhii, M. Ryzhii and H. C. Liu, *J. Appl. Phys.,* **92,** 207, 2002.

[17] V. Ryzhii, M. Ryzhii and H. C. Liu, *J. Appl. Phys*., **91**, 5887, 2002.

[18] V. Ryzhii and H. C. Liu, *Jpn. J. Appl. Phys*., **38**, 5815, 1999.

[19] M. Ryzhii and V. Ryzhii, *IEEE Trans. Electron Devices*, **47,** 1935, 2000.

[20] M.Artaki, *Appl. Phys. Lett.,* **52** (2), 141, 1988.

[21] R. K. Cook and J. Frey, *IEEE Trans. Electron Devices*, **ED-29,** 970, 1982.

[22] R. A. Warriner, *Solid-State Electron Devices*, **1,** 105, 1977.

[23] M. Artaki and I. C. Kizilyalli, *Appl. Phys. Lett*., **58,** 2467, 1991.

[24] M. Ryzhii and V. Ryzhii, *Physica E,* **7,** 120, 2000.

[25] M. Ryzhii and V. Ryzhii, *Jpn. J. Appl. Phys*., **38,** 5922, 1999.

[26] M. Ryzhii M and V. Ryzhii, *Appl. Phys. Lett*., **72,** 842, 1998**.**

[27] M. Ryzhii, I. Khmyrova and V. Ryzhii, *Jpn. J. Appl. Phys*., **37**, 78, 1998.

[28] M. Ryzhii, V. Ryzhii and M. Willander, J. *Appl. Phys*., **84,** 3403, 1998.

[29] M. Ryzhii, V. Ryzhii and M. Willander, *Jpn. J. Appl. Phys*., **38,** 6650, 1999.

[30] M. Ryzhii, V. Ryzhii, R. Suris and C. Hamaguchi, *Jpn. J. Appl. Phys*., **38**, L1388, 1999.

[31] M. Ryzhii, V. Ryzhii, Suris R and C.Hamaguchi, *Semicond. Sci. Technol*., **16,** 202, 2001.

[32] V. Ryzhii and M. Ryzhii, *Physical Review B*, **62**, 10292, 2000-I.

[33] O. O. Cellek, "Modeling, Fabrication, and Characterization of Quantum Well Infrared Photodetectors and Focal Plane Arrays," *Ph. D. Prestudy Report*, Middle East Technical University, Dept. of Electrical and Electronics Eng., 2003.

[34] O. O. Cellek and C. Besikci, *Semicond. Sci. Technol*., **19**, 183, 2004.

[35] O. O. Cellek, S. Memis, U. Bostanci, S. Ozer, C. Besikci, *Physica E,* **24**, 318, 2004.

[36] H. A. Gebbie, J. R. Harding, C. Hilsum, A. W. Pryce, and V. Roberts, *Proceedings of the Royal Society London,* **A206***,* 87,1951.

[37] A. Rogalski and K. Chrzanowski, *Optoelectronics Review*, **10**, 111, 2002.

[38] A. Rogalski, *Progress in Quantum Electronics*, **27**, 59, 2003.
[39] A. Rogalski, *Infrared Physics & Technology*, **43**, 187, 2002.

[40] R. D. Jr. Hudson, *Infrared Systems Engineering*, John Wiley & Sons, New York.

[41] P. Eriksson, J. Y. Andersson and G. Stemme, *Physica Scripta*, **T54**, 165, 1994.

[42] P. Eriksson, J. Y. Andersson and G. Stemme, *Sensors and Maretials*, **9**, 117, 1997.

[43] E. S. Barr*, American Journal of Physics*, **28**, 42, 1960.

[44] E. S. Barr, The infrared pioneers-II. Macedonio Melloni, *Infrared Physics*, **2**, 67, 1962.

[45] E. S. *Barr, Infrared Physics,* **3***,* 195, 1963.

[46] J. Leijtens, A. Court, J. H. Hoegee, *ICMENS*, 402-408, 2004.

[47] W. D. Lawson, S. Nielson, E. H. Putley, A. S. Young, *Journal of Physics and Chemistry of Solids*, **9**, 325, 1959.

[48] P. Norton, *Opto-Electron. Rev.,* **10**, 159, 2002.

[49] H. Sakaki, *Jpn. J. Appl. Phys.,* **19**, L735, 1980.

[50] Y. Arakawa and H. Sakaki, *Appl. Phys. Lett.,* **40**, 939, 1982.

[51] A. C. Gossard (ed), *Epitaxial Microstructures, Semiconductor and Semimetals*, (Academic, San Diego), **40**, 1994.

[52] X. Q. Liu, N. Li, F. Li, W. Lu, S. C. Shen, Y. Fu, M. Willander, H. H. Tan, C. Jagadish, and J. Zou, *Jpn. J. Appl. Phys.,* **39**, 5124, 2000.

[53] H. C. Liu, M. Gao, J. McCaffrey, Z. R. Wasilewski and S. Fafard, *Appl. Phys. Lett*., **78**, 79, 2001.

[54] S. Kim, H. Mohseni, M. Erdtmann, E. Michel, C. Jelen, and M. Razeghi, *Appl. Phys. Lett*., **73**, 963, 1998.

[55] S. Kim, M. Erdtmann and M. Razeghi, *Proc. SPIE,* **3629**, 371, 1999.

[56] S. Kim, M. Erdtmann and M. Razeghi, *J. Korean Phys. Soc*., **35**, 303, 1999.

[57] B. F. Levine, K. K. Choi, C. G. Bethea, J. Walker, and R. J. Malik, *Appl. Phys. Lett.*, **50**, 1092, 1987.

[58] C. A. Kukkonen, M. N. Sirangelo, R. Chehayeb, M. Kaufmann, J. K. Liu, S. B. Rafol, S. D. Guanpala, *Infra. Phys. Technol*., **42**, 397, 2001.

[59] B. F. Levine, C. G. Bethea, G. Hasnain, V. O. Shen, E. Pelve, R. R. Abbott and J. Hsieh, *Appl. Phys. Lett.,* **56**, 851, 1990.

[60] V. Jandhyala, D. Sengupta, E. Michielssen, B. Shanker, G. Stillman, *Applied Physics Letters,* **73**, 3495, 1998.

[61] H. Shneider, M. Walther, C. Schonbein, R. Rehm, J. Fleissner, W. Pletschen, J. Braunstein, P. Koid, G. Weimann, J. Ziegler and W. Cabanski, *Physica E,* **7**,101, 2000.

[62] Y. –C Chang and R. B. James, *Phys. Rev*. B, **39**,12 672, 1989.

[63] B.F. Levine, *J. Appl. Phys*., **74**, pp. R1, 1993.

[64] S.D. Gunapala and K.M.S.V. Bandara, *Thin Films*, **21**, 113, 1995.

[65] S.S.Li, *J. Chinese Ins. Elec. Eng*, **2**, 37, 1995.

[66] M. Z. Tidrow and K. Bacher, *Appl. Phys. Lett*., **69**, 3396, 1996.

[67] X. Jiang, S.S. Li, *IEEE Journal of Quantum Electronics*, **35**, No. 11, 1685, 1999.

[68] A. Y. Cho, *The Technology and Physics of Molecular Beam Epitaxy*, New York: Plenum Press, 1995.

[69] M. Razeghi, *The MOCVD Challenge Vol.1*. Bristol: Adam Hilger , 1989.

[70] M. Razeghi, *The MOCVD Challenge Vol.1*. Bristol: Adam Hilger , 1995.

[71] M. Henini, M. Razeghi, *Handbook of Infrared Detection Technologies,* Elsevier Science Ltd., 2002.

[72] Selçuk Özer, "InSb and InAsSb infrared photodiodes on alternative substrates and InP/InGaAs quantum well infrared photodetectors: pixel and focal plane array performance", METU, 2005.

[73] A. Rose, *Concept in Photoconductivity and Allien Problems*, Interscience, New York, 1963.

[74] A. Zussman, B. F. Levine, J. M. Kuo, and J. Jong, *J. Appl. Phys.*, **70**, 5101, 1991.

[75] S. D. Gunapala, S. V. Bandara, J. K. Liu, E. M. Luong, S. B. Rafol, J. M. Mumolo, D. Z. Ting, J. J. Bock, M. E. Ressler, M. W. Werner, P. D. LeVan, R. Chehayeb, C. A. Kukkonen, M. Levy, N. LeVan, M. A. Fauci, *Proceedings of SPIE,* **4028**, 262, 2000.

[76] S. D. Gunapala and S. V. Bandara, "Quantum Well Infrared Photodetector (QWIP) Focal Plane Arrays", *Semiconductors and Semimetals*, **62**, 197, Academic Press, 1999.

[77] H.C. Liu Appl. Phys. Lett. **60,** 1507 (1992).

[78] B. Xing, H. C. Liu, P. H. Wilson, M. Buchanan, Z. R. Wasilewski and J. G. Simmons, *J. Appl. Phys*. **76**, 1889, 1994.

[79] A. van der Ziel, *Functional Phenomena in Semiconductors*, Butterworths, London, 1959.

[80] R. Dornhaus and G. Nimtz, *Narrow-Gap Semiconductors*, **98,** 119, Berlin: Springer, 1983.

[81] L. C. West, S. J. Eglash, *Appl. Phys. Lett.*, **46**, 1156, 1985.

[82] D. Sengupta, V. Jandhyala, S. Kim, W. Fang, J. Malin, P. Apostolakis, K. C. Hseih, Y. C. Chang, S. L. Chuang, S. Bandara, S. Gunapala, M. Feng, E. Michielssen, and G. Stillman, *IEEE J. of Selected Topics in Quantum Electronics*, **4**, 746, 1998.

[83] M.A. Kinch and A. YAriv, *Applied Physics Letters*, **55**, 2093, 1989.

[84] B. F. Levine, C. G. Betha, G. Hasnain, V. O. Shen, E. Pelve, R.P. Abbott, and S.J. Hieh, *Applied Physics Letters*, **56,** 2093, 1990.

[85] S.R. Andrews and B.A. Miller, *Journal of Applied Physics*, **70**, 993, 1991.

[86] S. D. Gunapala, S. V. Bandara , J. K. Liu, W. Hong, E. M. Luong, J.M. Mumolo, M. J. McKelvey, D. K. Sengupta, A. Singh, C.A. Scott, R. Carrajelo, P. D. Maker, J. J. Bock, M. E. Ressler, M. W. Werner and T. N. Krabach, *Proc. SPIE*, **3379**, 382, 1998.

[87] K. K. Choi, *The Physics of Quantum Well Infrared Photodetectors,* Singapore: World Scientific, p.279, 1997.

[88] M. Ershov, S. Satou and Y. Ikebe, *J. Appl. Phys.,* **86**, 6442,1999.

[89] M. Ryzhii, I. Khmyrova, and V. Ryzhii, *IEEE Trans. Electron. Devices.,* **45**, 293, 1998.

[90] J. L. Pan and C.G. Fonstad, *IEEE J. Quantum Electronics* **35** 1673 (1999).

[91] Sa'ar, C.Maemelstein, H. Schneider, C. Schoenbein and M. Walther, *IEEE Photon.Technol. Lett*., **10** 1470, 1998.

[92] E. Rosencher, F. Luc, Ph. Bois, and S. Delaitre, *Appl.Phys. Lett*., **61,** 468, 1992.

[93] F. Stern and S. Sarma, *Phys. Rev. B*, **30**, 840, 1984.

[94] J. L. Thobel, A. Sleiman, P. Bourel, and F. Dessenne, J. Appl. Phys. **80,** 928, 1996.

[95] R.W. Hockney and J. W. Eastwood,*Computer Simulation Using Particles*, Bristol and New York: Adam Hilger, 1988.

[96] M. A. Khalil, M. Goano, A. Champagne, and R. Maciejko*, IEEE Photon. Technol. Lett.,* **8**, 19, 1996.

[97] J. L. Educato, J. P. Leburton, J. Wang, and D. W. Bailey, *Phys. Rev.B*, **44**, 8365, 1991.

[98] S. M. Goodnick, and P. Lugli, *Phys. Rev. B*, **37,** 2578, 1988.

[99] C. Besikci, A. T. Bakir, and B. Tanatar, *J. Appl. Phys,.* **88,** 1504, 2000.

[100] S. Datta, *Quantum Phenomena,* Addison-Wesley, Reading, MA, 1989.

[101] D. Schroeder, IEEE *Transactions on Computer-Aided Design*. **9,** 1136 (1990).

[102] R. Liboff, *Introductory Quantum Mechanics*, Addison Wesley Longman 1997.

[103] D. Gunapala, S. V. Bandara, J. K. Liu, E. M. Luong, N. Stetson, C. A. Shott, J. J. Bock, S. B. Rafol, J. M. Mumolo, and M. J. Mckelvey, *IEEE Trans. Electron Devices,* **47,** 326 (2000).

[104] Adachi, *J. Appl. Phys*., **58,** R1 (1985).

[105] K. Choi, *J. Appl. Phys*., **73,** 5230 (1993).

[106] R. Brown, S. J. Eglash, and K. A. McIntosh, *Optoelectronic Properties of Semiconductors and Superlattices*, **1,** edited by M. Razeghi Gordon and Breach Science Publishers, Amsterdam, p.353, 1996.

[107] D Gunapala, J.K. Liu, J.S. Park, M. Sundaram, C.A. Shott, T. Hoelter, T. Lin, S.T. Massie, P.D. Maker, R.E. Muller and G. Sarusi*, IEEE Trans. Electron Devices,* **44**, 51, 1997.

[108] F. Levine, A. Zussman, S. D. Gunapala, M. T. Asom, J. M. Kuo, and W. S. Hobson, *J. Appl. Phys.,* **72,** 4429, 1992.

[109] Schneider, C. Mermelstein, R. Rehm, C. Schonbein, A. Sa'ar, and M. Walther, *Phys. Rev. B*, **57,** R15096, 1998.

[110] Sarusi, S. D. Gunapala, J. S. Park, and B. F. Levine*, J. Appl. Phys*. **76,** 6001, 1994.

[111] R. Rehm, H. Schneider, M. Walther, and P. Koidl, *Appl. Phys. Lett*., **80,** 862 2002.

[112] R. Rehm, H. Schenider, K.Schwarz, M. Walther, P. Koidl and G. Weimann, *Proc. SPIE,* **4288**, 379, 2001

[113] Jelen, S. Slivken, T. David, M. Razeghi, and G. J. Brown, *IEEE J. Quantum Elect.,* **34,** 124, 1998.

[114] A. Beck, *Appl. Phys. Lett*., **63,** 3589 (1993).

[115] F. Levine, A. Zussman, J. K. Kuo, and J. de Jong, J. Appl. Phys. **71,** 5130 (1992).

[116] A. T. Bakir, "Advanced Monte Carlo Modeling of III-V Field-Effect Transistors", *M.S. Thesis*, Middle East Technical University, 1999

[117] S. Özer, "Performance Assessment of Pseudomorphic MODFETs Through Monte Carlo Simulations", *M.S. Thesis*, Middle East Technical University, 2000

[118] P. Sotirelis, P. Allmen, and K. Hess, *Phys. Rev. B*, **47**, p.12744, 1993

[119] B. K. Ridley, *J. Phys. C: Solid State Phys.,* **15**, 5899, 1982.

[120] K. Hess, *Appl. Phys. Lett.*, **35**, 484, 1979

APPENDIX A

SCATTERING RATES

This Appendix includes the calculation of the 3D and 2D scattering rates used in the Monte Carlo simulations [116, 117].

A.1 3D Polar Optical Phonon Scattering Rates

The polar optical phonon scattering rate is given by

$$\frac{1}{\tau_{pop}} = \frac{q^2(\frac{1}{2m^*})^{\frac{1}{2}}\omega_0}{4\pi\varepsilon\hbar}\left(\frac{1}{\varepsilon_{inf}} - \frac{1}{\varepsilon}\right)\frac{1+2\alpha E'}{\gamma^{\frac{1}{2}}(E)} F_0(E,E_0)(N_0 + \frac{1}{2} \pm \frac{1}{2}), \qquad \text{(A.1)}$$

$$N_0 = \frac{1}{e^{\frac{\hbar w_0}{k_B T}} - 1}, \qquad \text{(A.2)}$$

$$F_0(E,E') = \frac{1}{C}\left[A \ln\left|\frac{\gamma^{\frac{1}{2}}(E) + \gamma^{\frac{1}{2}}(E')}{\gamma^{\frac{1}{2}}(E) - \gamma^{\frac{1}{2}}(E')}\right| + B \right], \qquad \text{(A.3)}$$

$$A = \left[2(1+\alpha E)(1+\alpha E') + \alpha(\gamma(E)+\gamma(E'))\right]^2, \qquad \text{(A.4)}$$

$$B = -\alpha\gamma^{1/2}(E)\gamma^{1/2}(E')\left[4(1+\alpha E)(1+\alpha E') + \alpha(\gamma(E)\gamma(E'))\right], \qquad \text{(A.5)}$$

$$C = 4(1+\alpha E)(1+\alpha E') + (1+2\alpha E)(1+2\alpha E')\,. \tag{A.6}$$

After scattering, the electron energy updates are as follows,

$$E' = E \pm \hbar\omega_0\,, \tag{A.7}$$

$$\frac{\hbar^2 k^2}{2m_n^*} = E(1+\alpha_n E) \equiv \gamma(E)\,, \tag{A.8}$$

where ω_0 stands for the optical phonon frequency and + and – refer to absorption an emission, respectively.

The polar optical phonon scattering is not isotropic. Therefore, the angle β between the old k vector and the new k' vector after a scattering event is found from

$$\cos(\beta) = \frac{1+f-(1+2f)^{r_n}}{f}\,, \tag{A.9}$$

$$f = \frac{2\sqrt{EE'}}{\left(\sqrt{E}-\sqrt{E'}\right)^2}\,, \tag{A.10}$$

where r_n stands for a uniformly distributed random number between 0 and 1.

A.2 Acoustic Phonon Scattering Rate

The electron energy change for the acoustic phonon scattering is smaller than that of other phonon scattering mechanisms. The scattering rate is given as

$$\frac{1}{\tau_{NAP}} = \frac{(2m^*)^{\frac{3}{2}} D_a^2 k_B T}{2\pi\rho v_s^2 \hbar^4} \gamma^{\frac{1}{2}}(E)(1+2\alpha E)\left[\frac{(1+2\alpha E)^2 + \frac{1}{3}(\alpha E)^2}{(1+\alpha E)^2}\right], \qquad \text{(A.11)}$$

where v_s stands for the sound velocity in the crystal and D_a for the acoustic deformation potential.

The angle β is calculated from

$$\cos(\beta) = \frac{\left[(1+2\alpha E)^3(1-r_n)+r_n\right]^{\frac{1}{3}} - (1+\alpha E)}{\alpha E}, \qquad \text{(A.12)}$$

This scattering mechanism is treated as an elastic process.

A.3 Ionized Impurity Scattering Rate

The ionized impurity scattering rate and the angle β are given as

$$\frac{1}{\tau_{ION}} = \frac{N_i q^4}{32\pi\sqrt{2m^*}\varepsilon^2} \frac{1}{C(k)(1+C(k))} \frac{1+2\alpha E}{E^{3/2}(1+\alpha E)^{3/2}}, \qquad \text{(A.13)}$$

$$\cos(\beta) = 1 + \frac{2(r_n - 1)}{1 + \frac{r_n}{C(k)}}, \qquad \text{(A.14)}$$

$$C(k) = \left(\frac{1}{2L_D k}\right)^2, \qquad \text{(A.15)}$$

$$L_D = \sqrt{\frac{ek_B T}{q^2 N_i}}, \qquad \text{(A.16)}$$

where L_d stands for the Debye length, and N_i for the impurity density.

A.4 Intervalley and Intravalley Scattering Rates

The scattering rate from i^{th} valley to j^{th} valley is given as

$$\frac{1}{\tau_{INT}} = \frac{Z_j \, \mathrm{D}_{ij}^2 (m_j^*)^{3/2}}{\sqrt{2}\pi\rho\hbar^3\omega_{ij}} \gamma_j^{1/2}(E')(1+2\alpha E')(N_{ij} + \frac{1}{2} \mp \frac{1}{2}), \tag{A.17}$$

where D_{ij} stands for the intravalley deformation potential between the i^{th} and j^{th} valleys, Z_j for the equivalent j^{th} valley number, ρ for the mass density, and $\hbar\omega_{ij}$ for the intravalley photon energy. After scattering, the electron energy is

$$E' = E + \Delta E_{ij} \pm \hbar\omega_{ij}, \tag{A.18}$$

$$N_{ij} = \frac{1}{e^{\frac{\hbar\omega_{ij}}{k_B T}} - 1}, \tag{A.19}$$

where ΔE_{ij} stands for the conduction band energy difference. By using the above formula, the equivalent inter-valley scattering rates can be found by replacing j with 1 and Z_j with (Z_{j-1}). Since this scattering mechanism is isotropic, β is calculated as

$$\cos(\beta) = 1 - 2r_n. \tag{A.20}$$

A.5 2D Polar Optical Phonon Scattering Rates

The polar-optical phonon scattering rates are calculated using the Fermi's Golden Rule as [118, 119]

$$\Gamma_{ij}(k)=\frac{e^2 w_{LO}}{2}\left(n_B(w_{LO})+\frac{1}{2}\pm\frac{1}{2}\right)\int d^2q\frac{H^{eff}_{jiij}(q)}{q}\delta(E_i(k)\mp w_{\mathrm{LO}}-E_j(k\mp q)), \quad \text{(A.21)}$$

where the upper signs for the emission and the lower ones for the absorption. $n_B(w_{LO})$ stands for the Bose distribution function which gives the average number of phonons with energy $\hbar w_{LO}$ at temperature T. H^{eff} stands for effective interaction defined in terms of the dielectric matrix to add dielectric screening effects.

$$H_{ijkl}(q)=\sum_{mn}\varepsilon_{ijnm}(q,w=0)H^{eff}_{mnkl}(q). \quad \text{(A.22)}$$

Without screening effects the subband form factors are given by

$$H_{ijkl}(q)=\int_0^\infty dz\int_0^\infty dz' e^{-q|z-z'|}\phi_i(z')\phi_j(z')\phi_k(z)\phi_l(z). \quad \text{(A.23)}$$

With screening effect the dielectric matrix is calculated by the random phase approximation (RPA) by,

$$\varepsilon_{ijnm}(q)=\delta_{im}\delta_{jn}-V_{ijnm}(q)\chi_{nm}(q), \quad \text{(A.24)}$$

where $\chi_{nm}(q)$ stand for the static polarizability. The form factors and the Coulomb interaction matrix elements are related by $H_{ijkl}(q)=V_{ijkl}(q)/(2\pi e^2/q)$. In the work presented in this thesis, only the static dielectric function is considered. The usual Thomas-Fermi screening corresponds to the $q\rightarrow 0$ limit of our

dielectric function. The static screening approximation adopted here should be appropriate for large carrier densities, since $\hbar w_{LO}$ remains small compared with the characteristic energy (i.e. plasmon energy) of the electron gas.

A.6 2D Acoustic Phonon Scattering Rates

The acoustic phonon scattering rate is given by

$$\frac{1}{\tau_{ij}} = \frac{m^* k_b T E_1^2}{\hbar^3 \rho v_{sl}^2} \int F_i^2(z) F_j^2(z) dz, \tag{A.25}$$

where $F_i(z)$ and $F_j(z)$ stand for envelope wave functions, E_1 for the deformation potential constant, ρ for the density, and v_{sl} for the longitudinal sound velocity.

A.7 2D Impurity Scattering Rates

In doped regions of a semiconductor device, the carrier motion is disturbed by scattering due to ionized impurities distributed randomly. In our simulation, we considered two different types of 2D impurity scattering; remote ionized impurity scattering and background ionized impurity scattering [117].

A.7.1 Remote Ionized Impurity Scattering Rate

There are two kinds of charged scattering centers: quantum well dopants, which are the scattering centers in the well, and remote scattering centers, which are due to the impurities outside the well. In our program, the approach of Hess [120] is used to calculate the scattering rates due to both background and remote impurities.

Scattering rate due to remote impurities can be expressed as [120]

$$\frac{1}{\tau} = \frac{4\pi e^4 m^* N_R}{\hbar^3 \varepsilon^2 k} \int_0^{\pi} \frac{\exp(-4kz_0 \sin\theta)\sin\theta \, d\theta}{(2k\sin\theta + S)^2}, \tag{A.26}$$

where z_0 stands for the separation distance from the doped layer to the maximum of the square of the wave function, N_R for the remote impurity density, m* for the effective mass, ε for the relative dielectric constant of the semiconductor, k for the absolute value of two dimensional wave-vector, and S for the two dimensional screening constant. S is expressed as

$$S = \frac{e^2 n_{2d}}{2kT\varepsilon\varepsilon_0}, \tag{A.27}$$

where n_{2d} stands for the two dimensional carrier density, ε and ε_0 for the permittivities of the layers and free space respectively.

A.7.2 Background Ionized Impurity Scattering Rate

The background ionized impurity scattering rate for the electrons in the quantum well is given by [120]

$$\frac{1}{\tau} = \frac{4\pi e^4 m^* N_B}{\hbar^3 \varepsilon^2 k} \int_0^{\pi} \frac{\sin\theta d\theta}{(2k\sin\theta + S)^2}, \tag{A.28}$$

where N_B stands for the background impurity density. This impurity density depends on position of the particle in the well.

APPENDIX B

CALCULATION OF THE MOMENTUM AFTER SCATTERING

After every scattering, both the magnitude and direction of the particle's momentum should be updated [116, 117]. Magnitude of the particle's momentum is a function of energy difference before and after the scattering and expressed as

$$p' = \sqrt{2m^* \times (E + \Delta E)}\,, \tag{B.1}$$

where p' stands for the momentum after scattering, E for the carrier's energy before scattering and ΔE for the change in energy associated with the type of the scattering event selected.

If the scattering is isotropic (i.e., if the scattered electron has the same probability of being in any direction after scattering), the components k'_x, k'_y and k'_z can be found by considering that the probability density $p'(\phi', \theta')$ $d\phi' d\theta'$ is proportional to the number of available states on a sphere of radius k′, where ϕ' and θ' are the azimuthal and polar angles of $\mathbf{k'}$ with respect to k_z^L.

$p(\phi',\theta')$ equals $\sin\theta'$, since any ϕ' is equally probable. Therefore, ϕ' and θ' can be determined using uniformly distributed random numbers between 0 and 1. The relations between the azimuthal, polar angles and random numbers are expressed as

$$\phi' = 2\pi r_n , \tag{B.2}$$

$$\cos(\theta') = 1 - 2r_m , \tag{B.3}$$

After ϕ' and θ' are selected using random numbers r_n and r_m, components of the wave vector are obtained using the following equations:

$$k_x' = k' \times \sin\theta' \times \cos\phi' , \tag{B.4}$$

$$k_y' = k' \times \sin\theta' \times \cos\phi' , \tag{B.5}$$

$$k_z' = k' \times \cos\theta' . \tag{B.6}$$

The above expressions are only valid for the case of isotropic scattering. For anisotropic scattering processes, such as impurity scattering and polar optical phonon scattering, the final state $\mathbf{k'}$ is denoted by θ and ϕ, which are the polar and azimuthal angles of $\mathbf{k'}$ with respect to the initial wave vector $\mathbf{k}$. The azimuthal angle ϕ can also be determined randomly because the transition rate is independent of ϕ. Thus, ϕ can be found from

$$\phi = 2\pi r_n . \tag{B.7}$$

Polar angle θ is expressed as

$$\cos\theta = 1 - \frac{2r_m}{1 + (1 - r_m)\left(\frac{2k}{q_D}\right)^2} \quad \text{for impurity scattering,} \tag{B.8}$$

$$\cos\theta = \frac{1 + f - (1 + 2f)^{r_m}}{f} \quad \text{for polar optical phonon scattering.} \tag{B.9}$$

When updating the orientation of the electron wave vector **k** in a laboratory frame $\left(k_x^L, k_y^L, k_z^L\right)$, it is convenient to work with a new frame $\left(k_x^r, k_y^r, k_z^r\right)$, in which the k_z-axis is parallel to the initial wave vector **k**. The new frame is obtained by rotating $\left(k_x^L, k_y^L, k_z^L\right)$ by an angle α about the k_x-axis and then β about the k_z-axis, as shown in Figure B.1.

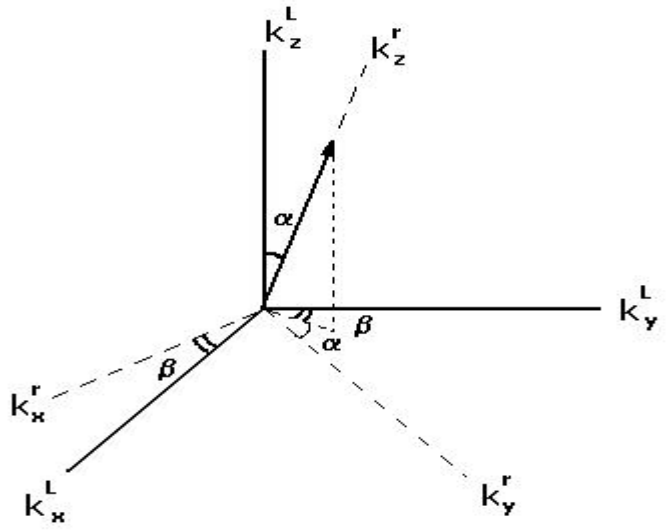

Figure B.1 Relation between the initial frame and new frame.

As the result of this rotation, the components of the wave vector after scattering in terms of the $\left(k_x^L, k_y^L, k_z^L\right)$ frame are obtained as

$$\begin{pmatrix} k_x' \\ k_y' \\ k_z' \end{pmatrix} = \begin{pmatrix} \dfrac{k_y}{\sqrt{k_x^2 + k_y^2}} & \dfrac{k_x k_z}{k\sqrt{k_x^2 + k_y^2}} & \dfrac{k_x}{k} \\ \dfrac{-k_x}{\sqrt{k_x^2 + k_y^2}} & \dfrac{k_y k_z}{k\sqrt{k_x^2 + k_y^2}} & \dfrac{k_y}{k} \\ 0 & \dfrac{-\sqrt{k_x^2 + k_y^2}}{k} & \dfrac{k_z}{k} \end{pmatrix} \begin{pmatrix} k' \sin\theta\cos\phi \\ k' \sin\theta\sin\phi \\ k' \cos\theta \end{pmatrix}. \qquad \text{(B.10)}$$

APPENDIX C

MATERIAL PARAMETERS

Material parameters [104, 105, 106] which are used in our simulations as follows;

for GaAs :

Table C.1: Material parameters for GaAs I.

valley	Effective mass × 9.11e-31 kg	Non-parabolicity factor (1/eV)	# of equivalent valleys
Γ	0.067	0.610	1
L	0.222	0.461	4
X	0.580	0.204	3

Table C.2: Material parameters for GaAs II

Intervalley deformation potential (D_0)	eV/cm
Γ↔Γ	0
Γ↔L	1×10^9
Γ↔X	1×10^9
L↔L	1×10^9
L↔X	5×10^8
X↔X	7×10^8

Table C.3: Material parameters for GaAs III

Acoustic deformation potential (Ξ_d)	eV
Γ	7.00
L	9.20
X	9.27

Table C.4: Material parameters for GaAs III

Intervalley phonon energy	eV
Γ↔Γ	0
Γ↔L	0.0278
Γ↔X	0.0299
L↔L	0.0290
L↔X	0.0293
X↔X	0.0299

Table C.5: Material parameters for GaAs IV

ρ (mass density):	5360 kg/m^3
υ_s (acoustic wave velocity):	5240 m/s
ε_s:	12.90 ε_0 (F/m)
ε_∞:	10.92 ε_0 (F/m)
E_g (Γ↔L):	0.290 eV
E_g (Γ↔X):	0.480 eV
Longitudinal optical phonon energy:	0.03536 eV

for $Al_xGa_{1-x}As$:

Table C.6: Material parameters for $Al_xGa_{1-x}As$ I

valley	Effective mass × 9.11e-31 kg	Non-parabolicity factor (1/eV)	# of eqv. valleys
Γ	0.067*(1-x)+0.126*x	0.610*(1-x)+0.4225*x	1
L	0.222*(1-x)+0.250*x	0.461*(1-x)+0.970*x	4
X	0.580*(1-x)+0.052*x	0.204*(1-x)+0.582*x	3

Table C.7: Material parameters for $Al_xGa_{1-x}As$ II

Intervalley deformation potential (D_0)	eV/cm
Γ↔Γ	0
Γ↔L	1×10^9
Γ↔X	1×10^9
L↔L	1×10^9
L↔X	5×10^8
X↔X	7×10^8

Table C.8: Material parameters for $Al_xGa_{1-x}As$ III

Intervalley phonon energy	eV
Γ↔Γ	0
Γ↔L	0.0278
Γ↔X	0.0299
L↔L	0.0290
L↔X	0.0293
X↔X	0.0299

Table C.9: Material parameters for $Al_xGa_{1-x}As$ IV

Acoustic deformation potential (Ξ_d)	eV
Γ	7.00*(1-x)+8*x
L	9.20*(1-x)+8*x
X	9.27*(1-x)+8*x

Table C.10: Material parameters for $Al_xGa_{1-x}As$ V

ρ (mass density):	(5.36-1.6*x)*1000 kg/m^3
υ_s (acoustic wave velocity):	5240 m/s
ε_s:	(13.18-3.12*x)*ε_0 (F/m)
ε_∞:	(10.89-2.73*x)*ε_0 (F/m)
E_g (Γ↔L):	0.29*(1-x)-0.25*x eV
E_g (Γ↔X):	0.48*(1-x)-0.585*x eV
Longitudinal optical phonon energy:	0.0343*(1-x)+0.047*x eV

CURRICULUM VITAE

Sema Memiş was born in 1972 in Ankara. She received her B.S. degree in Physic Education in 1996 and MS degree in Physics in 1998 at Middle East Technical University (METU). She worked as a research assistant from 1997 to 2004 in the Department of Physics, METU, Ankara.

PUBLICATIONS

1. .O.O. Cellek, S. Memis, U. Bostanci, S. Ozer, C. Besikci, *Physica E*, vol. 24, pp. 318–327, 2004.
2. S. Memis, O. O. Cellek, U. Bostancı, M. Tomak, C. Besikci, *Turk J. Phys*., to be published.

HOBBIES

Yoga, Movies, Bicycle, Reading, Sightseeing.